Supplementary Materials

Endocytosis caused by liquid-liquid phase separation of proteins

Louis-Philippe Bergeron-Sandoval[1], Hossein Khadivi Heris[2], Adam G. Hendricks[2], Allen J. Ehrlicher[2], Paul François[3], Rohit V. Pappu[4] and Stephen W. Michnick[1,5*]

correspondence to: S.W.M. (stephen.michnick@umontreal.ca).

This PDF file includes:

Materials and Methods

Figures S1 to S6

Tables S1 to S4

Captions for Movies S1 and S2

References

Other Supplementary Materials for this manuscript includes the following:

Movies S1
Movie S2

Materials and Methods

Strains and model system

We performed *in vivo* experiments in the *Saccharomyces cerevisiae* BY4741 *MATa his3Δ1 leu2Δ0 met15Δ0 ura3Δ0* background. To decouple the effects of turgor pressure on clathrin-mediated endocytosis (CME) we performed many experiments in a yeast strain with the gene for glycerol-3-phosphate dehydrogenase deleted, *GPD1Δ*. We acquired the *GPD1Δ* and other deletion strains from the Yeast Knock-out (YKO) deletion collection and GFP fluorescent strains from the Yeast GFP Clone Collection (Huh, Falvo et al. 2003), were generous gifts from J Vogel at McGill University. A complete list of strains used in this study are in Table S1.

Cell culture, gene manipulations and fluorescent reporters

Cells were normally grown to exponential phase (OD_{600} 0.1 to 0.6) in either rich medium (YPD) or low fluorescence medium (LFM) (Sheff and Thorn 2004). Liquid media or solid-agar cultures were incubated at 30°C. For 2-color imaging and other specific needs, the coding sequences for different fluorescent proteins were integrated into the genome, 3' to reporter protein open reading frames (ORFs) by homologous recombination (Tarassov, Messier et al. 2008). In short, mCherry and Venus YFP tags were integrated *via* homologous recombination by amplifying the HPH or NAT resistance cassettes from the respective pAG32 or pAG25 vectors with primer tails homologous to flanking sequences to the respective loci. BY4741, *GPD1Δ* or other YKO strains were then transformed with the respective PCR cassettes, selected for HPH or NAT resistance in YPD medium and confirmed by diagnostic PCR.

Truncation and site-directed mutagenesis within ORFs

Integration of the coding sequence for fluorescent protein Venus YFP by homologous recombination into the genome was also used to truncate the prion-like domains (PLDs) sequences in the ORFs of Sla1, Ent1, Ent2, Yap1801 and Yap1802. In order to truncate the required gene fragments, the Venus YFP coding sequence was integrated at precise locations prior to the STOP codon. The amino acid sequences that are deleted in each PLD truncation mutant are; Sla1 (1170-1245*Δ*), Ent1 (214-455*Δ*), Ent2 (255-615*Δ*), Yap1801 (355-630*Δ*) and Yap1802 (321-569*Δ*).

To generate proline substitution point mutations within or near PLDs of Sla1 and Ent2; we cloned synthetic gene fragments (GenScript) that coded for the mutations into the respective MoBy-ORF p5472 plasmids of our target genes (Ho, Magtanong et al. 2009). The respective position of proline mutations, gene fragment size and restriction enzymes are; Sla1 G1224P, Q1227P, A1231P, F1234P (842 bp, NarI and XmaI); Ent2 R359P, Q362P, H366P, L369P, L385P, L388P, K401P, E404P, L408P, Q411P, L415P, Q418P (1395 bp, XhoI and AflII). Standard cloning procedures with matching restriction enzymes were used to build the constructs and we confirmed final constructs by sequencing. Respective deletion strains were then complemented with either the proline-mutated or original p5472 plasmids.

Diffraction-limited fluorescence microscopy

For most experiments, cells were grown in LFM to an OD_{600} of ~0.1 to 0.6 and plated on either Nunc glass bottom 96-well plates (Thermo Scientific; 164588), glass bottom 8-well plates (Ibidi) or glass bottom 35 mm round dishes (MatTek). We used concanavalin A (Sigma-Aldrich ConA # C-7275) as a cell surface binding agent. Each well was loaded with 1mg/ml final concentration of ConA solution at room temperature for 15 minutes. ConA was then removed and wells were completely air dried before cells were added. Fluorescence images were acquired with distinct imaging platforms;

For the assessment of PLD truncations, we imaged cells on a Nikon TE2000 inverted microscope equipped with a 100X/1.45 plan APO lambda oil objective (Nikon), X-Cite lamp source (Excelitas), respective FITC (Chroma 41001HQ), EYFP (Chroma 49003ET) and mCH/TR (Chroma 49008ET) dichroic cubes and a Cool SNAP HQ camera. Z-stacks were acquired through a micron deep region with 5 planes and presented by maximal Z-projection.

For the measurements of lucifer yellow fluorescent probe uptake and cell sizes under different osmotic pressures, fluorescence images were collected on an InCell 6000 automated confocal microscope configured with a 100x/0.9 Plan FLUOR objective (Nikon) and 488 nm laser diode and FITC 525/20 emission filter for GFP fluorescence or 561 nm DPSS laser and dsRed 605/52 emission filter (GE healthcare life sciences). Single or two-color images were collected sequentially on a single focal plane with an exposure time of 100 msec. and a confocal slit of 2 AU. Image analysis and signal automated segmentation was performed with the InCell Developer software (GE healthcare life sciences) and the data was further analyzed and plotted in the R environment.

For other imaging data, the Quorum Diskovery platform was used in widefield, confocal and super-resolution imaging modes. Our Quorum Diskovery platform consists of a Leica DMi6000 inverted microscope equipped with a Diskovery multi-modal imaging system (Spectral) attached to either a Hamamatsu EM X2 camera or ORCA FLASH 4.0 V2 digital CMOS camera. Wide field or confocal excitation are achieved with a Spectral laser merge module with mounted 405 nm, 440 nm, 488 nm, 561 nm, and 640 nm diode pumped solid state laser sources linked to a Borealis beam conditioning unit. Images were acquired with a HCX PL APO 63x /1.47 NA oil corrected TIRF objective (Leica). This platform was remote controlled by the Metamorph software (Molecular Devices) and images were acquired and analyzed trough distinct pipelines. For particle tracking and mean squared displacement analyses, we used the Wave Tracer plugin to localize fluorescent foci centroid position through a wavelet algorithm and tracks particles in times stacks to calculate particles movement.

Fluorescent probes to quantify endocytosis or detect amyloid structures

Lucifer yellow (LY; Life technologies) assays to quantify endocytosis were performed at a final concentration of 1 mg/ml in YPD medium. Cells were incubated with the LY for 20 min or more. We then centrifuged at 3000 x g and washed cells 3 times in phosphate buffered saline (PBS; 137 mM sodium chloride, 10 mM phosphate, 2.7mM potassium chloride) before imaging in PBS with excitation wavelength (λ_{ex}) of 428 nm and emission wavelength (λ_{em}) of 536 nm. Measurements were taken from multiple cells in a single sample and this experiment was replicated 6 times.

The lipophlic stryryl dye FM4-64 (*N*-(3-Triethylammoniumpropyl)-4-(6-(4-(Diethylamino) Phenyl) Hexatrienyl) Pyridinium Dibromide) (Life technologies) was used to monitor plasma membrane uptake and staining of vacuolar membranes. Plasma membrane was labeled with 10 to 20 μM FM4-64 in YPD media and cells were incubated for 5 to 120 min. Cells were washed once in PBS and resuspended in LFM for imaging. FM4-64 stained cells were quantified by fluorescence microscopy (λ_{ex} of 510 nm, λ_{em} of 750 nm) on our Quorum platform (see Diffraction-limited fluorescence microscopy section).

We determined whether Sla1-mCherry puncta were labeled with the amyloid binding dye thioflavin T (ThT) in both live and fixed cells. Live cell ThT staining was performed as described by Kroschwald and collaborators (Kroschwald, Maharana et al. 2015). Cells grown to OD_{600} ~0.6 were harvested and resuspended in 30 μM ThT, 10 mM Tris/EDTA buffer (pH 7) for 20 min. Cells were then washed 3 times in PBS and resuspended in LFM media for imaging. Fluorescence microscopy (λ_{ex} of 405nm, λ_{em} of 450/50 nm) or (λ_{ex} of 488 nm, λ_{em} of 525/50 nm) were performed on the Quorum platform (see Diffraction-limited fluorescence microscopy section). BY4741 cells transformed with the plasmid pRS416-GAL-Sup35NM-RFP and induced for 2 hours in 2% galactose LFM were used as positive ThT stain controls. Alternatively, we confirmed ThT *in vivo* results with ThT staining of fixed cells. Cells were fixed with 4% paraformaldehyde 2% sucrose PBS for 20 min and washed once in PBS. Cells were then permeabilized with 0.1% Triton-X phosphate buffered (pH 7.5) detergent solution, and treated with 0.001% ThT for 10 min at room temperature. ThT stained cells were washed at 3–4 times with PBS and imaged on the Quorum platform (λ_{ex} of 488 nm, λ_{em} of 525/50 nm) (see Diffraction-limited fluorescence microscopy section). This experiment was replicated 3 times.

Cell treatment with water-glycerol solutions, 1,6 hexanediol and latrunculin-A

Water and glycerol binary combinations were mixed to obtain solutions with precise osmotic pressures ranging from 1.4 MPa to 30 MPa. Cells were grown to log phase, centrifuged for 2 minutes at 3000 x g and resuspended in the different water-glycerol binary solutions in Nunc 96-well glass bottom imaging plates (Thermo Scientific; 164588). Fluorescence images of *GPD1Δ* cells, that express EGFP from a pAG416-GPD plasmid, were then captured immediately after resuspension and at 1 hour intervals with the confocal InCell6000 (see Diffraction-limited fluorescence microscopy section). Intensity thresholding of the GFP channel allowed us to

segment the cells and obtain cell area values. These area values were used as a proxy for cell size at the different osmotic pressures. Measurements were taken from respective water-glycerol samples, this experiment was replicated 3 times.

We utilized 1,6-hexanediol (HD) to differentiate phase separated intracellular bodies from stable solid or fibrillar protein aggregates or to modulate the interactions among proteins that compose the endocytic condensate. HD is thought to change the solvent quality inside cells resulting in disruption of the interactions favorable to liquid-liquid phase separation. 1,2,3-hexanetriol (HT) was used as a negative control in all the HD assays. We treated cells grown to mid-log phase (OD_{600} 0.6) with HD or HT from 0 to 10 % wt/v and we measured both the uptake of fluorescent probes and progression of CME protein accumulation at cortical foci by fluorescence microscopy. Sla1-GFP signal at cortical sites in the presence of HD was assessed on the Quorum platform (see Diffraction-limited fluorescence microscopy section). HD dose-response was replicated 3 times.

Inhibition of F-actin synthesis was achieved using Latrunculin A (Lat A) at concentrations determined by titrating Lat A from 0 to 200 μM. Cells were treated for 20 minutes prior to measurements of the uptake of membrane (FM6-64 dye) and formation of Abp1-mCherry fluorescence foci. Lifetime of Abp1-mCherry at cortical sites in the presence of HD was assessed on the Quorum platform (see Diffraction-limited fluorescence microscopy section) and kymographs were generated with the Metamorph image analysis software (Molecular Devices). The Lat A dose-response curve indicated that a concentration of 20 μM Lat A was sufficient to impair actin nucleation at cortical sites. We replicated this experiment 4 times. We used a concentration of 20 μM Lat A in all our experiments unless mentioned otherwise.

Measurement of vesicle leakage of carboxyfluorescein by 1,6-hexanediol

Vesicles containing carboxyfluorescein were produced through drying, hydration, and extrusion steps. Briefly, 0.483 mg of DOPC (Avanti Polar Lipids) and 0.007 mg of Texas Red DHPE (Life Technologies) were dried on the walls of a test tube under N_2 followed by 30 min of vacuum. Dried lipids were hydrated with 2 ml of 20 mM carboxyfluorescein (~20x the self-quenching concentration in Figure S2D) in 20 mM HEPES at pH ~7.39 for 2.25 h at ~60 °C. The resulting multilamellar vesicles were gently vortexed and then extruded in 17 passes through 100 nm pores at room temperature to make unilamellar vesicles. Unencapsulated carboxyfluorescein was removed on a Sephadex G25 size exclusion column. To produce enough sample for triplicate experiments, the procedure above was conducted twice in parallel. Yields from both runs were combined and diluted with HEPES to a final volume of 6 ml of vesicle solution. Vesicle rupture or leakage causes carboxyfluorescein concentrations to fall below the self-quenching limit, resulting in increased fluorescence. Carboxyfluorescein solutions were made in 20 mM HEPES buffer. Fluorescence was monitored with a LS-50B spectrometer (Perkin Elmer), which excited the sample at 492 nm and measured emission at 512 nm via integration for 60 s through slits widths of 15 nm. The intensity of the first data point was set to 100 (in arbitrary units). Vesicle leakage

experiments were conducted in triplicate. For each run, emission at 512 nm was measured three times across a 1.0 cm path length cuvette containing 2 ml of vesicle solution to which stock solutions of 70% 1,6-hexanediol were added in order to reach 2-12% of 1,6-hexanediol by weight. Mixing was achieved by pipetting. To verify that pipetting did not disrupt vesicles, two methods were compared. For one of the three cuvettes, the solution was mixed by gently drawing 100 μl of solution into a standard 200 μl pipette tip three times. For the other two cuvettes, the solution was mixed by gently drawing 1 ml of solution into a 1 ml pipette tip that had been cut to widen the opening and decrease shear. Results from the two methods were indistinguishable. Data were normalized such that a solution with no 1,6-hexanediol has an intensity of 1.0. Control experiments were conducted in which vesicles were exposed to a high concentration (1.1%) of the surfactant Triton-X, such that all carboxyfluorescein leaked out of vesicles and was fully de-quenched.

Direct stochastic optical reconstruction microscopy (dSTORM)

Direct stochastic optical reconstruction data was acquired with the custom-imaging platform built by Quorum Technologies (see Diffraction-limited fluorescence microscopy section). Sample preparation for dSTORM was performed according to Ries, *et al*. with minor modifications (Ries, Kaplan et al. 2012). Cells were grown to an OD_{600}= 0.1 and plated on ConA coated glass bottom 35 mm round dishes for 10 minutes. Cells were then fixed with 4 % paraformaldehyde 2% sucrose PBS for 15 min. Fixation was stopped with two sequential incubations of 10 minutes in 50 mM NH_4Cl PBS and cells were further permeabilized and blocked in 0.25 % Triton X-100, 5 % BSA, 0.004 % NaN_3 PBS for another 30 minutes. We used GFP-Booster-Atto647N nanobodies (Chromotek; code gba647n) to label Sla1-GFP at a concentration of 10 µM in 0.25 % Triton X-100, 1% BSA, 0.004 % NaN_3 PBS for 60 minutes. Cells were washed extensively in PBS before imaging in blinking buffer 150 mM Tris-HCl pH 8.0, 30 mM β-mercaptoethylamine (MEA), 0.5 % glucose, 0.25 mg/ml glucose oxidase and 20 µg/ml catalase. We acquired streams of 10,000 to 20,000 frames at 30 msec. exposures and we used Wave Tracer plugin (Molecular Devices) to detect and gate events with a 16-bit intensity threshold of 1,000. Measurements were taken from distinct samples to reach a count of 250 bodies and this experiment was replicated 5 times. When possible we didn't use gain on the EMCCD camera to better calculate resolution; the camera has a conversion factor of 6e/count when no gain is used. Based on photon counts, we estimate an x, y-resolution of ≈10 nm with the 647 nm wavelength Atto647N fluorophore and a z-resolution of ≈50 nm with the astigmatic lens in 3D configuration calibrated on TetraSpeck beads (ThermoFisher). Center of mass for each event was calculated and we reconstructed images in Wave Tracer before further analysis in Metamorph (Molecular Devices). Sla1 structures were separated in circular and narrow elliptical shapes that correspond respectively to structure within or at the equator of cells.

Fluorescence recovery after photobleaching

Fluorescence recovery after photobleaching (FRAP) experiments (for recovery of Sla2-GFP and dextran-FITC) were performed on a Leica SP8 laser scanning confocal microscope (Leica). Images

were acquired with a 60x oil objective and the FRAP module within the LASX confocal software (Leica). A photobleaching 488 nm laser was pulsed for 190 to 650 msec. on samples, followed by acquisition of fluorescence recovery for 1 min with time resolution between 1.5 to 5 frames per seconds. GFP or FITC signal recovery was measured within either a segmented Sla1-mCherry or Syp1-mCherry region of interest to ensure that FRAP was acquired within the endocytic condensate. We also measured recovery in neighbor cytosol regions to assess recovery of dextran-FITC outside condensates. Analysis of the images intensity (I) fluctuations and segmentation of regions of interest (ROI) were performed on the LASX imaging software (Leica). Recovery measurements were taken from distinct samples. We replicated the dextran-FITC experiment 6 times and the Sla2-GFP recovery 4 times. We analyzed the data as follows:

We first applied a double normalization on bleached ROI1:

$$I(t)_{dbl\ norm} = \left(\frac{\frac{1}{n_{pre}} \cdot \sum_{t=1}^{n_{pre}} I(t)_{ROI\ 2'}}{I(t)_{ROI\ 2'}} \right) \cdot \left(\frac{I(t)_{ROI\ 1'}}{\frac{1}{n_{pre}} \cdot \sum_{t=1}^{n_{pre}} I(t)_{ROI\ 1'}} \right); \qquad (1.1)$$

, where ROI2 is a non-bleached region and n_{pre} is the number of pre-bleached images. We then used (1.2) results to perform a full-scale normalization:

$$I(t)_{full\ norm} = \frac{I(t)_{dbl\ norm} - I(t_{post})_{dbl\ norm}}{I(t_{post})_{dbl\ norm}} \qquad (1.2)$$

, where the first post bleach data time points are given a value of zero. We finally fitted each normalized trace with a non-least square function to best fit the single term equation:

$$f(I) = I_0 - a \cdot e^{-\omega t}\ ; \qquad (1.3)$$

from which we extracted mobile fractions and half recovery times for the Sla2-GFP and dextran-FITC samples. Analyses were performed using subroutines of the R package.

DHFR PCA procedure

We performed the DHFR PCA procedure has previously described (Tarassov, Messier et al. 2008) with minor modifications for a selected subarray of 30 potential Sla1 interactors from Biogrid. *MAT***a** strains harbouring either *Sla1-DHFR-F[1,2]-nat1* or *Sla1-ΔPLD-DHFR-F[1,2]-nat1*fusions were grown in liquid YPD supplemented with 100 μg/mL nourseothricin in a square v-bottom 96-well array block (3960; Corning). Each *MAT***a** strain was distributed in 3 rows by 10 columns arrangement to obtain 6 rows by 10 columns array on a single 96-well block. Another block array (6 rows by 10 columns arrangement) of 30 different *MAT***α** strains with *ORF.X-DHFR-*

F[3]-hph fusions was cultured in liquid YPD with 250 μg/mL hygromycin B. The strains were grown in liquid array for 24 hours at 30°C. Mating procedure was performed in a 96-well liquid array (6 rows by 10 columns arrangement) for 24 hours at 30°C. Each *MAT***a** and *MAT***α** strains were combined one-to-one in fresh liquid YDP without selection for mating, so that each resulting diploid strain had respective genes tagged with either of the DHFR fragments. The array was then transferred in quadruplicate in a 1,536-format using a robotically manipulated 384-pin tool (0.787 mm flat round-shaped pins, custom AFIX384FP3 BMP Multimek FP3N, V&P Scientific Inc., San Diego, CA) to synthetic complete agar plates (omnitrays, Nunc™) without lysine and without methionine and with 100 μg/mL nourseothricin and 250 μg/mL hygromycin B and were incubated for 48 h at 30°C to select for diploid cells. This step was repeated to further select for diploid cells using a robotically manipulated 1,536-pin tool (0.457 mm flat round-shaped pins, custom AFIX1536FP1 BMP Multimek FP1N, V&P Scientific Inc., San Diego, CA) to transfer the array on fresh plates. For selective growth, the strains were printed in 1,536 format on SC agar medium without adenine (pH 4.8) containing 4 % (w/v) Noble agar, 2 % (w/v) glucose, 1.74 g/L YNB without ammonium sulfate, and methotrexate (200 μg/mL) to select for DHFR reconstitution with either *Sla1-DHFR-F[1,2]-nat1* or *Sla1-ΔPLD-DHFR-F[1,2]-nat1* baits. We repeated the methotrexate selection on 3 distinct replicate plates. Printed methotrexate plates were incubated at 30°C throughout the imaging process and individual plates were photographed each day for 7 days with a 4 megapixel Canon digital camera (Powershot A520). Quantification of colony growth was achieved as described in Stynen *et al*. 2018 (preprint available on bioRxiv) with a custom-made macro on imaging software Fiji (v1.45b) to extract the integrated density of each colony. Briefly, for each colony, a 17-by-17 pixel area was screened around an initial central position to find the central intensity gravity point. From this central point, we scanned for the first pixels with intensity values that equal background intensity in the left, right, bottom and up directions and used these cardinal coordinates to determine a new central pixel. We iterated this process to get the borders of the colony in all four directions and a final central pixel. An oval was created and analyzed for integrated density, which is the mean density times the area. Further analyses were performed using a custom-made script in R (v3.2.3). The integrated densities calculated in the previous section were log_2 transformed.

Phase separation and partitioning of fluorescent proteins in cleared cell lysates

Yeast cells that respectively express pellets were harvested and disintegrated by Y-PER reagent. Pellets were resuspended in the Y-PER reagent solution and incubated at room temperature with shaking for 20min. The homogenate was centrifuged at 20 000×g for 30min and the pellet was discarded (see Thermo scientific YPER protein extraction instructions). Homogeneous cleared cell lysates were titrated with PEG from 0 to 10% and monitored by confocal microscopy (see Quorum platform) for appearance of a condense droplet phase. Fluorescent signal from respective protein was acquired along the brightfield channel with a HCX PL APO 63x /1.47 NA oil corrected TIRF objective (Leica) and 50 μm pinhole spinning disk on our Quorum Diskovery platform (see Diffraction-limited fluorescence microscopy section).

Expression of chimeric Epsins, mammalian Epsin homologs and non-cognate PLDs

Sequence encoded information, shown by the meta-predictor PONDR-FIT(Xue, Dunbrack et al. 2010), suggest that yeast proteins Ent1 and Ent2 and their mammalian homologs EPN1 and EPN3 are in fact intrinsically disordered proteins (IDPs) with defined disordered (*low complexity*) domains that are conserved despite that the corresponding sequences not being conserved. For Ent1 and Ent2 the predicted disordered domains match with previous predictions for prion domains (PLDs) (Alberti, Halfmann et al. 2009).

We expressed homologous human proteins EPN1 and EPN3 in yeast. Human ORFs from the CCSB Human ORFeome library from Dana-Farber Cancer Institute (Dharmacon) were sub-cloned into the pAG yeast expression vectors with a fluorescent tag. Target ORF were cloned in the yeast gateway expression vector pAG416GDP-ccdB-EGFP (Addgene) from their respective pDONR entry plasmids. Sequence variants of Sup35 NM (Sup35 NM, Sup35 NM(N) and Sup35 NM(Q)) and Sla1 PLD were also cloned in the yeast gateway expression vectors pAG416GDP-ccdB-EGFP (Addgene) from their respective pDONR entry plasmids (generous gift from R Halfmann) and tested for colocalization with Sla1 condensates. Finally, ENTH domains of Ent1/ and EPN1/3 were cloned between the XbaI and SpeI sites of the pAG416GDP-*ORF.X*-EGFP vectors to create chimeric Epsin proteins with either the Sla1 PLD, Sup35 NM, Sup35 NM(N) or Sup35 NM(Q) moiety. We tested colocalization of each construct with the endocytic condensate (BY4741 SLA1-mCherry::*hph* cells) and functional complementation. Images were acquired with a HCX PL APO 63x /1.47 NA oil corrected TIRF objective (Leica) and 50 μm pinhole spinning disk on our Quorum Diskovery platform (see Diffraction-limited fluorescence microscopy section).

Centroid tracking of Sla1 foci

We measured the mean square displacement (MSD) of single Sla1-YFP fluorescent foci within a confocal volume on the Quorum platform (see Diffraction-limited fluorescence microscopy section). Images were acquired at 20 fps for 30 seconds with a 50 μm pinhole spinning disk and we performed particle centroid tracking with the Wave Tracer plugin in the Metamorph software (Molecular Devices). We included only foci that remained in the confocal volume throughout the acquisition and which showed decreasing fluorescence intensity as a function of MSD (Figure S4I). We next determined the linear displacement of the Sla1 foci towards the cell interior with the particle coordinates plotted as a function of elapsed time (Figure S4J). Measurements were taken from multiple cells in a single sample and this experiment was replicated 3 times.

Quantification of membrane in nascent vesicles under HD titration

We quantified the amount of membrane in single nascent CME vesicles by fluorescence emitted from FM6-64 labelled membrane. Overnight *GPD1*Δ Sla1-YFP cell cultures were diluted 1:40 in fresh LFM with HD concentrations from 0 to 5%. Cells were first incubated in 20 μM Lat A and then in the HD solutions for 5 minutes and then labelled with 5 µM FM4-64 for another 5 minutes before direct fluorescence image acquisition on the Quorum platform (see Diffraction-limited

fluorescence microscopy section). Single vesicles where segmented with an intensity threshold in both Venus YFP and FM4-64 channels to quantify the membrane fluorescence that co-localizes with Sla1 signal. Measurements were taken from multiple cells in a single sample and this experiment was replicated 5 times. Average intensity measurements per nascent vesicle were normalized to values between 0 and 1 for the whole HD treatment concentration range. As a reference point to compare with membrane invagination predictions, we extracted mean and standard deviation values from data for HD concentration below 2 %; mean and standard deviation were also determined for each HD concentration.

Effect of 1,6-hexanediol (HD) titration on condensate stability

Formation of a endocytic condensate results in an interface between the condensate and the cytosol and we can treat the condensate and the dispersed cytosol as two phases defined by an interface between them. In a mean field description, the cohesive interactions that drive the formation of the condensate derive from the balance of interactions amongst the condensate and cytosolic components. This will determine the stability of the condensate. In addition, the interface between the condensate and cytosol will be governed by an interfacial tension. A simple adaptation of the Flory-Huggins model for binary mixtures can be used to quantify the interfacial tension (Dill and Bromberg 2011).

The model is as follows: We shall define two condensed phases *viz.*, the condensate phase (D) and the cytosolic phase (C). The interfacial tension γ_{DC} defines the free energy penalty associated with increasing the interfacial area between the two phases. If $\gamma_{DC} > 0$, then the interfacial area will be minimized, thus resulting in spherical condensates. From the vantage point of the condensate, reducing the interfacial tension decreases the number of condensate components that are "sacrificed" to be at the interface and thus lose favorable intra-condensate interactions.

If the total free energy of the two bulk phases D and C and the interface between the phases is F, then the interfacial tension associated with changing the interfacial area A is defined as:

$$\gamma_{\mathrm{DC}} = \left(\frac{\partial F}{\partial A}\right)_{n_D, n_C, T} ; \qquad (2.1)$$

For simplicity, we shall use a mean-field model with the two phases defined on a lattice with coordination number z. The molecules of D and C will be considered to be of similar size and the translational entropy will be set to zero. If a is the area per molecular unit that is exposed to the interface, then equation (2.1) becomes:

$$\gamma_{\mathrm{DC}} = \left(\frac{\partial F}{\partial A}\right)_{n_D, n_C, T} = \left(\frac{\partial U}{\partial A}\right)_{n_D, n_C, T} = \frac{1}{a}\left(w_{\mathrm{DC}} - \frac{w_{\mathrm{DD}} + w_{\mathrm{CC}}}{2}\right); \qquad (2.2)$$

Here, the w terms are the effective mean-field energies associated with interactions between components of the condensate (w_{DD}), the cytosol (w_{CC}) and the components of the condensate and the cytosol (w_{DC}). These energies are in units of k_BT and the convention is that the energies are negative if they are favorable and positive if they are unfavorable. Accordingly, it follows that:

$$\begin{aligned} \gamma_{\mathrm{DC}} > 0 \text{ if } |w_{\mathrm{DC}}| < \left|\frac{w_{\mathrm{DD}} + w_{CC}}{2}\right| \\ \gamma_{\mathrm{DC}} = 0 \text{ if } |w_{\mathrm{DC}}| = \left|\frac{w_{\mathrm{DD}} + w_{CC}}{2}\right|; \\ \gamma_{\mathrm{DC}} < 0 \text{ if } |w_{\mathrm{DC}}| > \left|\frac{w_{\mathrm{DD}} + w_{CC}}{2}\right| \end{aligned} \tag{2.3}$$

Importantly, equation (2.2) can be rewritten in terms of the Flory-Huggins interaction coefficient using the relationship:

$$\chi_{\mathrm{DC}} = \frac{z}{k_BT}\left[w_{\mathrm{DC}} - \left(\frac{w_{\mathrm{DD}} + w_{\mathrm{CC}}}{2}\right)\right] = \left(\frac{c_E}{k_BT}\right); \tag{2.4}$$

Here, c_E is cohesive energy that holds the condensate together and represents the balance of condensate-cytosol, intra-condensate and intra-cytosol interactions. Accordingly,

$$\begin{aligned} \gamma_{\mathrm{DC}} = \frac{1}{a}\left(w_{\mathrm{DC}} - \frac{w_{\mathrm{DD}} + w_{\mathrm{CC}}}{2}\right) = \left(\frac{k_BT}{za}\right)\chi_{\mathrm{DC}}; \\ za\gamma_{\mathrm{DC}} = k_BT\chi_{\mathrm{DC}} \end{aligned} \tag{2.5}$$

Alternatively,

$$\chi_{\mathrm{DC}} = \left(\frac{za}{k_BT}\right)\gamma_{\mathrm{DC}} = \left(\frac{c_E}{k_BT}\right); \tag{2.6}$$

$$za = \left(\frac{c_E}{\gamma_{\mathrm{DC}}}\right)_{\mathrm{HD}=0\%}; \tag{2.7}$$

Note that the values of z and a are fixed by the lattice and components of the condensate. Through measurements combined with the Young-Laplace theory, we have estimates of the interfacial tension and c_E in the absence of HD – as shown in equation (2.7). These estimates can be used as shown in equation (2.7) to estimate the value of za. Since this value of za is independent of HD concentration, one can fix za and use the estimate of cohesive energy c_E at different HD concentrations to estimate the change in interfacial tension as a function of HD concentration using equation (2.8) below:

$$\gamma_{\mathrm{DC}}(\%\mathrm{HD}) = \left[\frac{c_E(\%\mathrm{HD})}{za}\right]; \tag{2.8}$$

Polystyrene beads and Dextran-FITC osmoporation

To incorporate dextran-FITC of different chain length inside haploid yeast *GPD1*Δ cells, we used an osmoporation technique similar to that described by da Silva Pedrini *et al*. (da Silva Pedrini, Dupont et al. 2014). Cells treated with Lat A were centrifuged for 2 minutes at 3000 x g and resuspended in a water-glycerol binary solution at 1.4 MPa for 30 minutes, then in a 30 MPa solution for 1 hour. Osmoporation of dextran-FITC is performed after these steps, by centrifuging cells at 3000 x g and resuspending the pellet in the 1.4 MPa water-glycerol solution with the dextran-FITC at 10 mg/ml for 1h. After this incubation period, cells were put on ice and washed 3 times with cold PBS with 20 μM Lat A. Cells were preserved on ice until they were plated on ConA treated 35 mm imaging dishes for 10 minutes and imaged on either the Quorum or Leica platforms (see Diffraction-limited fluorescence microscopy and Fluorescence recovery after photobleaching sections respectively).

We also incorporated 200 nm orange (540/560) FluoSpheres carboxylate-modified polystyrene beads (ThermoFisher) with this technique. Beads where either coated with 10 mg/ml BSA prio to incorporation into cells. After osmoporation, cells were preserved on ice until they were plated on ConA treated coverslips and mounted on glass imaging slides for subsequent image acquisition and optical tweezers experiments.

microNS-GFP micro-rheology

To determine the effect of *osmoporation* on the cell rheological properties, we measured displacement of expressed viral capsid microNS particles labeled with GFP in both normal and osmoporated cells (Figure S4A-F). Cells were transformed with the microNS-GFP pRS expression plasmid, a generous gift of S. Alberti at Max Planck Institute of Molecular Cell Biology and Genetics (MPI-CBG). microNS movement was recorded on the Quorum platform (see Diffraction-limited fluorescence microscopy section) within a 2 microns thick Z-stack of 5 confocal planes (50 μm pinholes) acquired at 5 frames per second (fps). Measurements were taken from multiple cells in a single sample and this experiment was replicated 3 times. Image analysis was performed with Metamorph and Wave Tracer plugin (Molecular Devices), to track particles displacement with centroid localization on maximum intensity projections. We further filtered the mean square displacement (MSD) data for particles that are confined and showed that they have MSD similar to the technical noise of our apparatus setup.

Optical tweezers measurements and calibration

Dynamic mechanical analysis of yeast cytoplasm was performed with a custom optical tweezers (OT) platform. Our OT system is an inverted microscope (Nikon Ti-E) equipped with a CFI APO SR TIRF 100x / 1.49 NA oil immersion objective (Nikon), a 1,064 nm Nd:YVO_4 10 W infrared laser (IPG Photonics), an X-cite lamp source (Excelitas) and a nano-positioning stage (Mad City Labs). Oscillation of the tweezers on the specimen plane from 0.1 Hz to 2000 Hz was achieved

with an acousto-optic deflector (AOD, AA Optoelectronics) coupled to a digital frequency synthesizer that we controlled with in house Labview (National Instruments) routines. Light transmitted through the specimen was collected with a condenser lens and reflected onto a position-sensitive detector (PSD) (Thorlabs, PDP90A) to perform back focal plane interferometry. Before acquisitions we adjusted the microscope for Köhler illumination and ensured that all the optics were conjugate to the respective specimen plane or back focal plane. At each frequency of excitation we recorded the signals (120,000 samples at 1000 Hz to 2,000,000 samples at 0.1 Hz at 20 kHz) and performed Fourier analysis. Measurement time for each frequency sweep was about 15 minutes on distinct samples and this experiment was replicated 2 times. For each sample, we covered the frequency domain from high-to-low frequencies, then we repeated the procedure from low-to-high to ensure consistent frequency response with prolonged laser exposure.

Calibration of the optical tweezers measures was performed as previously described with minor modifications (Fischer, Richardson et al. 2010, Hendricks, Holzbaur et al. 2012). Data analysis was conducted with in-house Matlab code. Data quality was first confirmed by assessment of the sinusoidal shape of the response to the applied stress. Traces with a coherence of 0.95 or greater were included in the analysis. We averaged 17 traces in distinct cellular locations and determined their trap stiffness k_{trap} (mean ± standard error; $8.0 \times 10^{-5} \pm 2.7 \times 10^{-5}$ N•m^{-1}), photodiode sensitivity factor β (mean ± standard error $10.7 \times 10^{3} \pm 2.3 \times 10^{3}$ nm•V^{-1}) and frequency-dependent viscoelastic moduli G' (storage) and G'' (loss) (Figure 4).

To account for the relaxation dynamics observed, we performed a fit on the forced response to sinusoidal oscillations and the power spectra of the spontaneous fluctuations of the bead to a model of a transiently crosslinked network of flexible polymers (Lieleg, Schmoller et al. 2009) .

$$G' = G_0 - a \cdot \frac{N k_{off}}{\frac{k_{off}^2}{4\pi^2} + f^2} + b \cdot \left(\frac{f}{f_0}\right)^{\alpha}; \quad (2.9)$$

$$G'' = c \cdot \frac{N f}{\frac{k_{off}^2}{4\pi^2} + f^2} + d \cdot \left(\frac{f}{f_0}\right)^{\alpha}; \quad (2.10)$$

From these fits, we extracted the average parameters (G_0; 16.53), (f_0; 37.44), number of crosslinks (N; 3×10^{14}), crosslink off-rate (k_{off}; 8.28), power law (α; 0.98) and constants ratios (a/b; 1.06×10^{-14}/2.19), (c/d; 1.33×10^{-14}/0.72). Deviation of α above a value 0.75 indicates that retraction or extension of entangled protein filaments ends could contribute to the relaxation mechanism (Koenderink, Atakhorrami et al. 2006).

Dimensions and geometry of membrane contour and endocytic condensates

From published data, we considered that the optimal membrane U-shaped geometry before vesicle excision is about 70 nm high and 60 nm wide (Idrissi, Blasco et al. 2012). To approximate the area and volume, the U-shape was decomposed into a hemispherical cap of 30 nm radius over a cylinder of 30 nm radius and 40 nm high. We then calculated, with these dimensions, an invaginated membrane area of 1.32 x 10^{-14} m^2 and volume of 1.70 x 10^{-22} m^3.

We also defined for the membrane bending energy, the invagination height profile as a function of position around the invagination peak and middle of the condensate;

$$h(x, y) = h_0 \cdot \exp\left(\frac{-(x^2 + y^2)}{2R_0^2}\right); \quad (3.1)$$

where h_0 is the invagination depth and R_0 is the radius of invagination.

To calculate the area and volume occupied by the endocytic condensate and thus the amount of displaced cytosol material, we used our dSTORM measurements. The hemispherical endocytic condensate volume was calculated to be 2.43 x 10^{-21} m^3 for a radius of 105 nm. The same hemispheric condensate has an area of 6.93 x 10^{-14} m^2. These dimensions agree with the size of ribosome exclusion zones observed surrounding invaginated clathrin patches observed by EM (Kukulski, Schorb et al. 2012).

Calculation of the energies that favor and counteract membrane invagination

We calculated the membrane bending energy with the standard Helfrich model for the membrane profile obtained by equation (3.1) and considered a membrane bending modulus κ_m of 12.5•K_BT (Helfrich 1973, Harmandaris and Deserno 2006, Carlsson and Bayly 2014):

$$U_{em} = 11\sqrt{\left(\frac{\pi^3}{32}\right)}\left(\frac{h_0}{R_0}\right)^2 \kappa_m; \quad (3.2)$$

We determined the energy required to generate a 70 nm deep invagination to be 3 x 10^{-18} J.

We considered that the viscoelastic cytosol behaves as a Kelvin-Voigt material and that the total stress is equal to the sum of the elastic and viscous stresses, such that:

$$\sigma = \varepsilon E_i + \dot{\varepsilon}\eta; \quad (3.3)$$

, where η is the cytosol viscosity at a specific frequency f_x obtained with:

$$\eta = \frac{G''}{2\pi f_x}; \quad (3.4)$$

For stringency, we used a Young's (or elastic) modulus (E) for the cytosol of 45 Pa (see Eq. 3.6 below) and calculated the deformation with the condensate radius (1.18 x 10^{-7} m) over the cell radius (2 x 10^{-6} m). We obtained an elastic stress of 3 Pa.

We next determined η at 0.5 Hz to be 0.35 Pa•s. and the deformation rate of 0.004 s^{-1}, for a condensate velocity v of 7.4 x 10^{-9} m•s^{-1} (Figure S4I,J).

$$\dot{\varepsilon} = \frac{v}{6\pi R_{drop}}; \quad (3.5)$$

, which gives a negligible viscous stress of 0.0014 Pa. With a volume of 2.42 x 10^{-21} m^3, the total stress of 3.0014 Pa corresponds to an energy cost of 7.26 x 10^{-21} J to displace the viscoelastic cytosol.

Endocytic condensate material properties and contact angle

We determined the values of the elastic modulus of the cytosol based on the observation that compressible biological materials have a Poisson's ratio (ν), which relates all material moduli to each other, of 0.45 (or between 0.3 and 0.5) (Zhang, Soman et al. 2013). We then used the relationship between shear modulus (G) and Young's (or elastic) modulus (E):

$$E_i = 2(1 + \nu_i)G_i; \quad (3.6)$$

to calculate an approximate elastic modulus of 45 Pa for the cytosol from the G' of 15 Pa at 1 Hz. This strain rate was used to consider a G' near the elastic plateau of the material response. With the volume of displaced cytosol and this modulus value, we could determine the mechanical stress imposed on the cytosol to be ~3 Pa (see Eq. 3.3-3.5). This corresponds to a compression force (F) of ≈1.4 x 10^{-13} N. We then isolated the equivalent modulus (E') from Hertz elastic contact equation

$$F = \frac{4}{3} E'_{ij} R'^{\frac{1}{2}}_{ij} \delta^{\frac{3}{2}}_{ij}; \quad (3.7)$$

into

$$E'_{ij} = \frac{4F}{3R'^{\frac{1}{2}}_{ij} \delta^{\frac{3}{2}}_{ij}}; \quad (3.8)$$

, where δ_{ij} is the interface indentation (or invagination depth), to estimate the respective elastic moduli of the cytosol and the condensate, again with both materials having a Poisson's ratio of 0.45. The equivalent modulus is determined by:

$$\frac{1}{E'_{ij}} = \frac{(1+\nu_i)^2}{E_i} + \frac{(1+\nu_j)^2}{E_j}; \tag{3.9}$$

where E_i and E_j are the respective elastic moduli of the objects in contact and

$$\frac{1}{R'_{ij}} = \frac{1}{R_i} + \frac{1}{R_j}; \tag{3.10}$$

for contact between two spheres of radii R_i and R_j. These relationships gave us a endocytic condensate elastic modulus of 59 Pa.

Given that gravity is negligible at the scales we are measuring, the condensate can be treated as a sectional arc of a sphere or hemispherical cap alone (Figure S1G) and we can estimate the condensate contact angle;

$$\theta = 2 \cdot \tan^{-1}\left(\frac{h}{d}\right) \tag{3.11}$$

, where d is condensate radius and h is condensate height. Based on our 2D dSTORM measures we obtained a contact angle of about 97°. Note that at the hundred nanometer scale, condensate wetting geometries are also affected by evaporation and line tension at the three-phase contact line.

Theoretical model based on elastic and adhesive contact mechanics

To explain how phase separation of disordered proteins into a 100 nm-scale viscoelastic body can invaginate the membrane (in the absence of turgor, F-actin polymerization and steric effects), we propose a model in which elastic and adhesive contact mechanics can generate enough energy (estimated from membrane bending to be $\approx 3 \times 10^{-18}$ J) to drive local invagination of the membrane.

We explored the idea that when endocytic condensates are nucleated between the membrane and cytoplasm, new interfaces are created and the free energy available on the condensate interfaces can produce work to deform both surrounding substrates (membrane and cytosol). We thus hypothesize that free energy is released upon phase separation and adhesion of the endocytic condensate to neighbor structures, which is converted into mechanical work. We describe below the details of the model.

We first propose a general model where the energy penalties to create interfaces around the condensate and deform the cytosol and the membrane follow a super-linear growth as a function of invagination depths δ (of both cytosol and membrane), whereas the free energy released by condensate phase separation is linear. We expressed the relationship between these two general energy terms and the total energy U with the power-law function:

$$U \sim \phi \cdot \delta^{1+\varepsilon} - \psi \cdot \delta; \tag{4.1}$$

, where ϕ is the energy penalty term, ψ is the available work and the exponent $\varepsilon > 0$. When δ is isolated from the partial derivative of equation (4.0), such as:

$$\frac{\partial U}{\partial \delta} = \phi(1+\varepsilon) \cdot \delta^{\varepsilon} - \psi;$$

$$\delta^{*} = \left(\frac{\psi}{\phi(1+\varepsilon)}\right)^{\frac{1}{\varepsilon}}; \tag{4.2}$$

, we observe that our model predicts that δ scales with ϕ and ψ:

$$\delta^{*} \sim \frac{\psi}{\phi}; \tag{4.3}$$

We provide below a proof for this model, where ϕ is decomposed into individual elastic, viscous friction and surface stress terms and ψ is fragmented in the work of adhesion from the respective condensates interfaces. We also describe the quantities contained within these individual terms; either directly measured, calculated or estimated.

Parallel to the membrane plane, surface energies formed by the condensate (D), cytosol (C) and membrane (m) come to equilibrium as described by Young's equation:

$$\gamma_{cm} = \gamma_{dm} + \gamma_{dc} \cdot \cos\theta; \tag{4.4}$$

With a contact angle of about 97°, the cytosol-membrane surface tension (γ_{cm}) is predicted to be approximately equal to the condensate-membrane surface tension (γ_{dm}). We determined the values of γ_{dc} and γ_{dm} next.

We used an apparent Young's modulus (E_{cell}) of 1 kPa, determined from atomic force microscopy on haploid yeast spheroblast (Munder, Midtvedt et al. 2016). We considered that this modulus represents the bulk material properties of both membrane and cytosol when deformed towards the cell interior, as for a CME-driven invagination. We then calculated the overall mechanical stress in the system with Hooke's law:

$$\sigma = \varepsilon E_i; \tag{4.5}$$

to create the U-shape membrane geometry observed by EM. The deformation ε of the membrane was decomposed to represent stretching of an elastic band, where deformation equals length difference over original length. For our U-shaped deformation the linear contour was established

at 174.2 nm, whereas the same membrane line measured ≈ 80 nm before invagination. This gives us a deformation of 1.18 (dimensionless) and a stress of 1178 Pa.

This mechanical stress corresponds to the pressure difference ΔP experienced by the cytoplasm and the membrane due to the presence of the endocytic condensate. This pressure difference arises from adhesive, hydrostatic and elastic stress energies. We then used the Young-Laplace equation:

$$\Delta P = 2\gamma_{dc} \cdot H \; ; \tag{4.6}$$

, where H is the mean curvature of the interface and is equal to $1/R_d$, to calculate γ_{dc} at the cytosol interface based on our observation that the condensate is circular in shape. Equation (4.6) determines the pressure difference across the condensate-cytosol curved interface as a function of surface energy, and gives a condensate/cytosol interfacial tension γ_{dc} of 7×10^{-5} N•m^{-1}.

Based on Young's equation (4.4) and the endocytic condensate-membrane contact angle θ value, the relationships between interfacial tensions is:

$$\gamma_{cm} = \gamma_{dm} + \gamma_{dc} \cdot \cos\theta$$
$$\gamma_{cm} = \gamma_{dm} - (8 \cdot 10^{-6}); \tag{4.7}$$

and

$$\gamma_{dc} > \gamma_{dm}; \tag{4.8}$$

where the condensate-membrane surface tension γ_{dm} can range between about 1.8 to 7×10^{-5} N•m^{-1}. The γ_{dm} limits also arise from equation (4.9) below.

The interfacial tension γ of a fluid condensate is inversely proportional to the square of the length ξ of its discrete elements (i.e. the individual biopolymers), we used this relationship to estimate maximal and minimal γ values:

$$\gamma = \frac{k_B T}{\xi^2}; \tag{4.9}$$

, where k_B is the Boltzmann constant and T is temperature in kelvin (Brangwynne, Mitchison et al. 2011). The interfacial tension values for protein based biological condensates (in which protein radii range from 1 to 10 nm) should be on the order of 1×10^{-4} N•m^{-1} and below.

To directly estimate the work of adhesion at the endocytic condensate interfaces, we used the Young-Dupré equation:

$$W_{dm} = \gamma_{dc} \cdot (1 + \cos\theta); \tag{4.10}$$

that implies a direct relationship between work of adhesion of an interface (W_{ij}), the condensate contact angle and the surface tension γ_{dc}. We could determine the work of adhesion at the membrane interface W_{dm} to be 6 x 10^{-5} N•m^{-1}.

We also combined the Young's equation (4.1) and the Dupré relationship:

$$W_{dc} = \gamma_{dm} + \gamma_{cm} - \gamma_{dc}; \qquad (4.11)$$

to express the work of adhesion at the endocytic condensate-cytosol interface W_{dc}:

$$W_{dc} = 2\gamma_{dm} + \gamma_{dc} \cdot (\cos\theta - 1); \qquad (4.12)$$

in terms of interfacial tension at endocytic condensate interfaces with both membrane and cytosol. We could thus estimate the maximal W_{dc} value to be 6 x 10^{-5} N•m^{-1}, if $\gamma_{dm} \approx \gamma_{dc}$.

We determined in parallel whether adhesion dominates the mechanical potential of endocytic condensates, as opposed to capillary effects. Under so called elasto-capillary action, condensate interfacial tension (Y) can deform an elastic sheet as a function of either condensate radius (R) or the thickness (h) and elastic modulus (E) of the slender material in contact with the condensate; in our case, the plasma membrane (Roman and Bico 2010). We can considered that the phospholipid bilayer membrane is about 10 nm thick and the cell has a bulk elastic modulus E of 1 kPa (Munder, Midtvedt et al. 2016). With a surface tension γ_{dc} of 7 x 10^{-5} N•m^{-1}, we determined that R is larger and h is about equal to the elasto-capillary length:

$$\frac{\Upsilon}{E}; \qquad (4.13)$$

, and the membrane sheet should remain undeformed at the 3-line contact point by interfacial tension alone (Figure 6A). This prediction is also consistent with EM data where the membrane doesn't bulge out under the Laplace pressure within condensates on cortical sites (Idrissi, Grotsch et al. 2008). In this scenario our system should obey the Young-Dupré equation and deformation can only come from work of adhesion.

Johnson-Kendall-Roberts (JKR) theory describes how non-flat surfaces stick together and conform to one another to minimize their interfacial energy (Johnson 1971). When they adhere to one another, soft and compliant materials such as the membrane and cytoplasm are subject to a deformation limited by elastic strain. Style, *et al*. adapted the JKR theory of contact mechanics to describe the contact surface geometry between a microscopic rigid particle and a soft substrate

(Style, Hyland et al. 2013); we followed a similar approach to estimate model 4.1 parameters and test our hypothesis.

If we consider the two condensate interfaces where deformation occurs, both membrane and cytoplasm, the energy penalty to create these curved surfaces (or interfaces) are equal to the sum of elastic, viscous and surface energies.

To build a complete energy model, the elastic energy penalties were determined with the JKR theory. Since the geometry of the contact surface corresponds to the endocytic condensate geometry itself, we calculated the elastic penalties U_{ely} to deform both interfaces as a function of invagination depth δ_{ij}:

$$U_{e|y}\left(\delta_{ij}, E'_{ij}, R'_{ij}\right) = cE'_{ij}R'^{\frac{1}{2}}_{ij} \cdot \delta_{ij}^{\frac{5}{2}}; \quad (4.14)$$

where E'_{ij} and R'_{ij} are calculated with (3.5) and (3.6) respectively and c is a constant.

$$c = \frac{8}{15} \cdot \sqrt{3}\,; \quad (4.15)$$

We incorporated a correction for the membrane elastic penalty to compensate for the reduced JKR accuracy at the hundred nanometer scale and for soft materials (Style, Hyland et al. 2013) by addition of the Helfrich Hamiltonian of membrane bending at individual δ_{ij} values. We substituted h_0 in equation (3.2.0) for δ_{ij} and used a fixed radius of invagination R_{ij} to get the relationship:

$$U_{em.corr}\left(\delta_{ij}\right) = 11\sqrt{\left(\frac{\pi^3}{32}\right)}\left(\frac{\delta_{ij}}{R_{ij}}\right)^2 \kappa_m; \quad (4.16)$$

We calculated a corrected energy cost of $\approx 1 \times 10^{-18}$ J to deform the membrane (Table S3). The cytoplasm elastic energy barrier did not require correction and we considered no elastic nor viscous condensate deformation in our model.

JKR theory is also less accurate for very soft materials and small particles because the model neglects surface stresses (Style, Hyland et al. 2013). Inclusion of energy penalties to increase surface length at the interfaces was proposed by Style *et al.* to compensate for this reduced accuracy (Style, Hyland et al. 2013). We incorporated the surface penalties (U_{ily}) for the formation of the new interfaces into our model with the function;

$$U_{i|y}\left(\delta_{ij}, \gamma_{ij}\right) = \pi\gamma_{ij} \cdot \delta_{ij}^{\,2} \quad (4.17)$$

, where the respective interfacial tensions γ_{dc} and γ_{dm} determine the energy cost to increase the interfacial areas. The energy to form the condensate/cytosol interface is ≈1 x 10^{-18} J and is equivalent to the combined elastic penalties. These energy values confirm that at the hundreds of nanometers scale, surface stress can dominate (or equate) elasticity in material responses to deformation. With this approach, we propose a more comprehensive model of the energy required to deform the membrane on cortical sites, that also takes into account creation of new surfaces and deformation of the cytosol.

We also incorporated an additional energy penalties $U_{v|y}$ to displace the viscous cytosol with the equation:

$$U_{v|y}\left(\delta_{ij}, R'_{ij}, \eta, \dot{x}\right) = \eta \dot{x} \delta_{ij} \cdot 6\pi R'_{ij}; \tag{4.18}$$

, where the displacement rate is the condensate maximum velocity of 7.4 x 10^{-9} m•s^{-1} (Figure S4I,J).

If the conversion of the energy released by adhesive contact into mechanical energy is above the total energy barrier, the condensate should drive membrane invagination. The extent of membrane invagination will be limited by the free energy available. For the purpose of our model, we calculated the energy of adhesion ($U_{a|y}$) with the JKR term:

$$U_{a|y}\left(\delta_{ij}, W_{ij}, R'_{ij}\right) = 2\pi W_{ij} R'_{ij} \cdot \delta_{ij}\ ; \tag{4.19}$$

where W_{ij} is the work of adhesion at each interface, as determined by equations (4.10) and (4.12), respectively. The work of adhesion refers to the energy released in the wetting process of the endocytic condensate on the membrane, it equals the work needed to separate the two adjacent phases and is given by the Dupré equation (4.11).

We then integrated the elastic (4.14, 4.16), interfacial (4.17), viscous (4.18) and adhesion (4.19) terms into a complete energy equation for i,j interfaces, where:

$$i = \{droplet\}; \quad j = \{membrane, cortex\}; \tag{4.20}$$

into

$$U_{total}(\delta_{dm}, \delta_{dc}, \gamma_{dm}, \gamma_{dc}, W_{dm}, W_{dc}) = cE'_{dm} {R'_{dm}}^{\frac{1}{2}} \cdot {\delta_{dm}}^{\frac{5}{2}} + 11\sqrt{\left(\frac{\pi^3}{32}\right)} \left(\frac{\delta_{dm}}{R_{dm}}\right)^2 \kappa_m + \pi\gamma_{dm} \cdot {\delta_{dm}}^2 - 2\pi W_{dm} R'_{dm} \cdot \delta_{dm} + cE'_{dc} {R'_{dc}}^{\frac{1}{2}} \cdot {\delta_{dc}}^{\frac{5}{2}} + \pi\gamma_{dc} \cdot {\delta_{dc}}^2 + \eta\dot{x} 6\pi R'_{dc} \cdot \delta_{dc} - 2\pi W_{dc} R'_{dc} \cdot \delta_{dc}; \tag{4.21}$$

To reduce the number of free fitting parameters, we first defined the values of the variables that were measured (or calculated) and expressed the work of adhesion of each interface W_{ij}, as determined by (4.10) and (4.12) respectively:

$$U_{total}(\delta_{dm}, \delta_{dc}, \gamma_{dm}) =$$
$$cE'_{dm}R'_{dm}{}^{\frac{1}{2}} \cdot \delta_{dm}{}^{\frac{5}{2}} + 11\sqrt{\left(\frac{\pi^3}{32}\right)}\left(\frac{\delta_{dm}}{R_{dm}}\right)^2 \kappa_m + \pi\gamma_{dm} \cdot \delta_{dm}{}^2 - \frac{7\pi R'_{dm}\gamma_{dc} \cdot \delta_{dm}}{4}$$
$$+cE'_{dc}R'_{dc}{}^{\frac{1}{2}} \cdot \delta_{dc}{}^{\frac{5}{2}} + \pi\gamma_{dc} \cdot \delta_{dc}{}^2 + \eta\dot{x}6\pi R'_{dc} \cdot \delta_{dc}$$
$$-\left(4\pi R'_{dc}\gamma_{dm} - \frac{9\pi R'_{dc}\gamma_{dc}}{4}\right) \cdot \delta_{dc}\,; \qquad (4.22)$$

Finally, we coupled the membrane and cytosol invagination or penetration depth δ_{ij} with a simple function:

$$\delta_{dc} \rightarrow f(\delta_{dm}) = \mu \cdot \delta_{dm} + k; \qquad (4.23)$$

, that reflects a mechanical coupling, where μ and k are constants that were solved for the (δ_{dm},δ_{dc}) coordinates (0,0) and (7 x 10^{-8}, 1.2 x 10^{-7}) to 1.7 and 0 respectively. This linear relationship between δ_{dm} and δ_{dc} ensures that a critical condensate volume is conserved and that invagination values are consistent with the distribution of condensate size and membrane invagination from imaging and EM data (Idrissi, Blasco et al. 2012). This single δ_{ij} variable was henceforth referred to as δ (without any index).

We ended with a total energy function with 2 independent variables:

$$U_{total}(\delta, \gamma_{dm}) = cE'_{dm}R'_{dm}{}^{\frac{1}{2}} \cdot \delta^{\frac{5}{2}} + 11\sqrt{\left(\frac{\pi^3}{32}\right)}\left(\frac{\delta}{R_{dm}}\right)^2 \kappa_m + \pi\gamma_{dm} \cdot \delta^2 - \frac{7\pi R'_{dm}\gamma_{dc} \cdot \delta}{4}$$
$$+cE'_{dc}R'_{dc}{}^{\frac{1}{2}} \cdot (\mu\delta)^{\frac{5}{2}} + \pi\gamma_{dc} \cdot (\mu\delta)^2 + \eta\dot{x}6\pi R'_{dc} \cdot (\mu\delta)$$
$$-\left(4\pi R'_{dc}\gamma_{dm} - \frac{9\pi R'_{dc}\gamma_{dc}}{4}\right) \cdot (\mu\delta); \qquad (4.24)$$

that expresses the total energy as a function of membrane invagination and interfacial tension of the endocytic condensate-membrane interface.

We explicitly defined the mechanical strain term of the model (4.1):

$$\phi \cdot \delta^{1+\varepsilon} = \left(\begin{array}{c} cE'_{dm}R'^{\frac{1}{2}}_{dm} + 11\sqrt{\left(\frac{\pi^3}{32}\right)}\left(\frac{\delta^{-\frac{1}{2}}}{R_{dm}{}^2}\right)\kappa_m + \pi\gamma_{dm}\cdot\delta^{-\frac{1}{2}} + cE'_{dc}R'^{\frac{1}{2}}_{dc}\mu^{\frac{5}{2}} \\ + \pi\gamma_{dc}\cdot(\mu\delta)^{-\frac{1}{2}} + \eta\dot{x}6\pi R'_{dc}\cdot(\mu\delta)^{-\frac{3}{2}} \end{array} \right) \cdot \delta^{\frac{5}{2}}; \quad (4.25)$$

, where the power law variable ε of 1.5 reflects the energy penalties for parabolic shaped cytosol and membrane deformations, and the mechanical work term of (4.1):

$$\psi \cdot \delta = \left(\frac{7\pi R'_{dm}\gamma_{dc}}{4} + \mu\left(4\pi R'_{dc}\gamma_{dm} - \frac{9\pi R'_{dc}\gamma_{dc}}{4}\right)\right)\cdot\delta; \quad (4.26)$$

We minimized the function (4.24) on the δ_{dm} (1 x 10^{-9}m to 7 x 10^{-9}m) and γ_{dm} interval (1.8 x 10^{-5}N•m^{-1} to 7 x 10^{-5} N•m^{-1}) and obtained an energy minimum. This corresponds to an energy optimal invagination of 41 nm with a maximal γ_{dm} of 7 x 10^{-5} N•m^{-1}. For the γ_{dm} value of membrane invagination is favorable up to a depth of 80 nm (Figure S6). We also determined that to achieve an energy favorable membrane invagination of 70 nm (total energy U_{total} equal or less than 0 J) the system requires a minimal γ_{dm} of 6 x 10^{-5} N•m^{-1} (Figure S6D). With this lower γ_{dm} value, the system would reach a minimum energy with a membrane invagination of 35 nm (Figure S6D).

With the geometric data and estimates of γ_{dc}, we determined the energy required to create new interfaces U_i around the condensate and the adhesive energy U_a at these interfaces (Figure 6B, S6 and Methods; Eq. 4.17,4.19). At a δ value of 41 nm (corresponds to energy minimum), we summed the energy penalties (ϕ term) and estimated a total energy barrier of 2.4 × 10^{-18} J to deform the membrane and cytosol in contact with the endocytic condensate. This energy cost includes the elastic, viscous, and interfacial stress penalties (Figure 6B and Methods; Eq. 4.25, Table S4). The interfacial stress penalty to form the condensate/cytosol interface is 1.0 × 10^{-18} J and is equivalent to the membrane elastic penalties. These results are consistent with studies of artificial materials where at the 100 nm scale, surface stress can dominate elasticity in material responses to deformation (Style, Hyland et al. 2013). When we consider the energy favourable domain, our model correctly predicts the magnitude of invagination (about 40 nm to 80 nm) that is accessible for a successful invagination that leads to vesicle excision (Figure 6C and S6).

To relate the free energy on the endocytic condensate interface to density of molecular interaction on the condensate surface, we divided the adhesion energy of 3 x 10^{-18} J at the cytosol interface by the protein density on the condensate surface. We estimated, based on our dextran exclusion experiment, that proteins on the condensate surface are arranged in a matrix with an average mesh size of 10 nm (or less). We used an average protein filament width of 2 nm and a condensate area of 6.93 x 10^{-14} m^2 to obtain a minimum of 1.4 x 10^3 protein segments on the condensate surface. To maximize the adhesive energy per protein exposed on the interface, we determined the minimum

amount of protein on the condensate surface to be about 2×10^{-21} moles and a maximal adhesive energy density of 1.3 $kJ•mol^{-1}$. Conversely, this approach gives a maximum of 2.8×10^{10} molecules on the surface, or 4.7×10^{-14} moles of proteins, and a minimal adhesive energy of 6.3×10^{-5} $J•mol^{-1}$. To be stringent, we considered the former.

Statistical analysis and software for microscopy

Software used in microscopy measurements and microscopy data analysis are also outlined in the methods details. For dSTORM images in Figure 1B, center of mass for each event was calculated and we reconstructed images in Wave Tracer before further analysis in Metamorph (Molecular Devices). For the measurements of fluorescent probe uptake (Figure 4A,C,D and S1E-F) and cell sizes under different osmotic pressures (Figure S1A), image analysis and signal automated segmentation was performed with the InCell Developer software (GE healthcare life sciences) and the data was further analyzed and plotted in the R environment. Quantification of FM4-64 membrane probe (Figure 2C and 6C) was performed with Metamorph image analysis software (Molecular Devices). When cell populations in Figure 2C and Figure 3D were compared for quantified fluorescence, we applied a Welch's two-sided t-test with sample sizes ($n = 100$) to achieve a power greater than 0.9 with a 95% confidence. Statistical analysis was done with the R software package. For particle tracking and mean squared displacement analyses in Figure S4, we used the Wave Tracer plugin with the Metamorph image analysis software (Molecular Devices) to localize fluorescent foci centroid position through a wavelet algorithm and tracks particles in times stacks to calculate particles movement. Kymographs in Figure S1 were also generated with the Metamorph image analysis software (Molecular Devices). Analysis of the images intensity (I) fluctuations and segmentation of regions of interest (ROI) for fluorescence recovery after photobleaching (FRAP) experiments (Figure 2E, 5E-F and S5C-D) were performed on the LASX imaging software (Leica). FRAP data was plotted using subroutines of the R package. Optical tweezers measurements were performed with in house Labview (National Instruments) routines and the data was analyzed with a custom Matlab (MathWorks) code.

Theoretical model based on elastic and adhesive contact mechanics

Calculations and graphics of the elastic, viscous, surface and adhesive energies in our model were performed in either Maple or the R software environment. The parameters, variables and relationships we used in the calculation are listed in Table S2 and S3. A summary of the invagination and energy results we obtained with these specific parameters are in Table S4.

Supplementary Figures

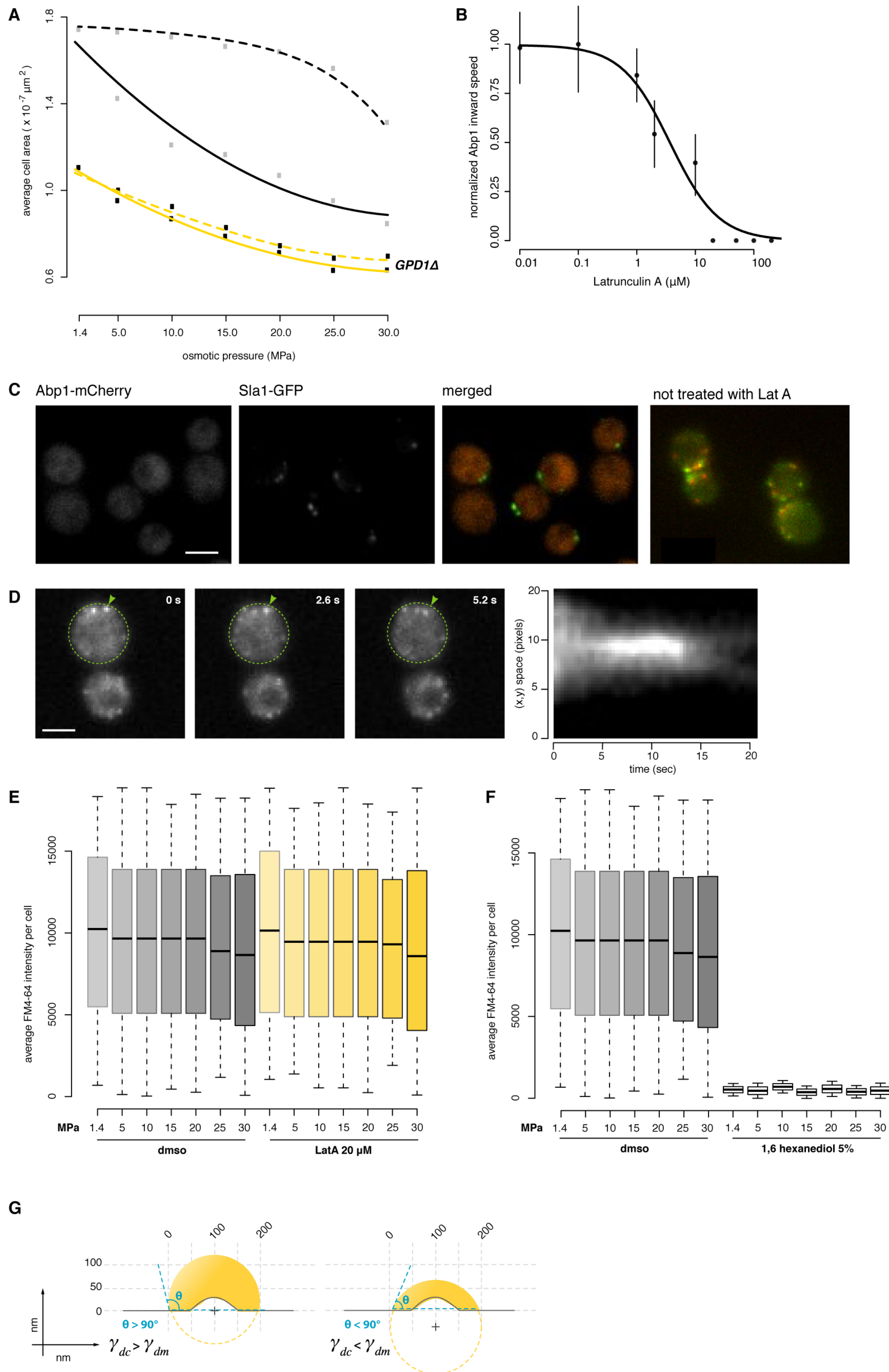

**Supplementary Figure 1 | ***GPD1Δ* cells cannot maintain turgor and undergo normal CME in the absence of actin polymerization (Latrunculin A-treated). Related to Figure 1. (A) To detect turgor

pressure and cell size adaptation to osmotic shock in wild type (black) and *GPD1Δ* strain (yellow), we monitored by fluorescent microscopy the cross-sectional area (μm^2) of shocked cells (solid lines) and adapted cells (dashed lines) in water-glycerol binary solutions from 1.4 MPa to 30 MPa. Points represent mean area values (n=200 cells). (B) Dose-response of normalized Apb1-mCherry inward speed as a function of Latrunculin A (Lat A) concentration (mean ± sd; n = 12; logistic fit). Apb1-mCherry tracks in time were analyzed from kymographs of the Lat A-treated cells. Note that Abp1-mCherry structures disappear at 20 μM Lat A and above. (C) F-actin polymerization is disrupted by Lat A. Assessment of Abp1-mCherry actin structures by fluorescence microscopy in cells treated with 20 μM Lat A for 5 min. Maximal intensity projections of Z-stacks of cells after and without treatment are shown, Sla1-GFP (green signal) and Abp1-mCherry (red signal). Scale bar 2 μm. (D) Time progression of Sla1-YFP structures (arrow) in *GPD1Δ* cells (dashed contour) treated with 20 μM Lat A (effective concentration determined in B-C). Elapsed time relative to focus appeareance is indicated is top right corners. Scale bar 2 μm. The kymograph in the right panel shows spatiotemporal progression of the Sla1-YFP focus identified by the arrow. (E) Membrane-associated FM4-64 fluorescent probe uptake was quantitatively assessed by fluorescence imaging. *GPD1Δ* strains undergo normal CME when treated with Lat A, (F) but not when treated with 1,6-hexanediol, n = 900 cells for each condition. (G) Endocytic condensate width (209 ± 10nm) and height (118 ± 6 nm) give a contact angle (θ) of ~ 97°.

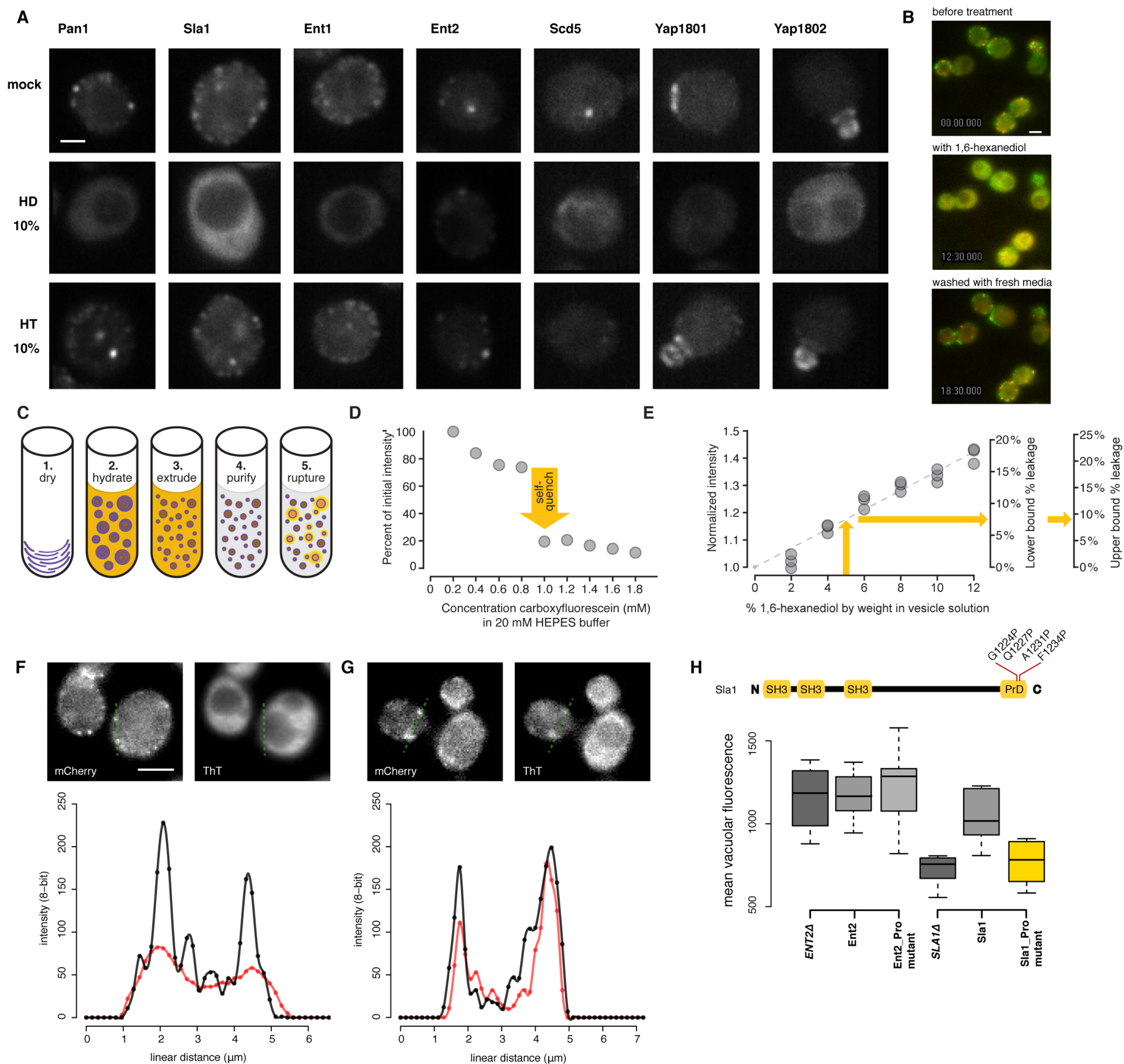

Supplementary Figure 2 | Cortical patch-associated PLD-containing proteins fail to form puncta in cells treated with 1,6-hexanediol (HD) and do not colocalize with Thioflavin T (ThT). Related to Figure 2 and Movie S1. (A) Fluorescence images of GFP-tagged Pan1, Sla1, Sla2, Ent1, Ent2, Scd5, Yap1801 and Yap1082 puncta 5 min after treatment with either DMSO, 1,6-hexanediol or 1,2,3-hexanetriol, images where acquired with InCell6000 confocal microscope. Scale bar 2 μm. (B) Pulse-chase experiments with HD show that HD-dependent dissolution of Sla1 puncta is reversible. Images from fluorescent monitoring through time of Sla1-GFP (green signal) and Abp1-mCherry (red signal) under a pulse-chase cycle of 10% HD. Low Fluorescence Medium (LFM) was replaced with 10% HD LFM at 10 min and replaced with fresh LFM at 15 min. Maximal intensity projections of Z-stacks are shown before HD treatment (left), 2.5 min after

incubation with HD (middle) and 3.5 min after HD removal (right). Scale bar 2 μm. See also Movie S1. (C) Protocol for determining vesicle leakage by 1,6-hexanediol. Vesicles containing carboxyfluorescein were produced through drying (Step 1), hydration (Step 2), and extrusion (Step 3). Dried lipids were hydrated with a 20 mM carboxyfluorescein solution (~20x the self-quenching concentration in panel D). Unencapsulated carboxyfluorescein was removed on a size exclusion column (Step 4). Vesicle rupture or leakage causes carboxyfluorescein concentrations to fall below the self-quenching limit, resulting in increased fluorescence (Step 5). (D) Carboxyfluorescein self-quenches at concentrations ≥ 1.0 mM in solution as seen by the sharp decrease in fluorescence intensity at 1.0 mM. Intensity of the first data point was set to 100 (in arbitrary units). (E) Vesicle leakage due to 1,6-hexanediol is minor. Carboxyfluorescein fluorescence intensity of vesicle solutions treated with 1,6-hexanediol (2 to 12% by weight). Standard deviations were smaller than the symbols in the graph (n = 3; repeated 3 times). Data were normalized such that a solution with no 1,6-hexanediol has an intensity of 1.0. A linear fit constrained to pass through (0, 1.0) is shown by the dashed line. Consistent with the data in panel D, full de-quenching resulted in a 2.95- to 3.34-fold increase in fluorescence. Propagation of this range of multipliers leads to the conclusion that for vesicles in 5% 1,6-hexanediol solutions (vertical arrow) only 7.5% (horizontal arrow, lower bound) to 9.0% (upper bound) of carboxyfluorescein leaks out of vesicles. (F) We observed no colocalization of Thioflavin T (ThT) with Sla1-mCherry puncta. Fluorescence microscopy of Sla1-mCherry (upper left), ThT stain (upper right) and line scan analysis (lower panel) for the dashed line in green. Scale bar, 2 μm (G) Fluorescence microscopy of Sup35-mCherry (upper left), ThT stain (upper right) and line scan analysis (lower panel) for the dashed line in green. Scale bar, 2 μm. (H) Mutations of PLDs that prevent phase separation of proteins also disrupt CME. Proline mutations were introduced near or within the C-terminal PLD domains of Sla1 and Ent2 mutant strains and CME measured by fluorescence of lucifer yellow dye uptake. Positions of the mutation are shown on the schematic representation of the protein Sla1. Introduction of such mutations into the PLDs of Sla1 resulted in equivalent effects of complete Sla1 deletion, and PLD deletion in Figure 2C, on CME-mediated lucifer yellow dye uptake into *GPD1Δ* background. Boxplots with n = 100 cells (center line, median; box, upper and lower quartiles; whiskers, 1.5x IQR; crosses, outliers).

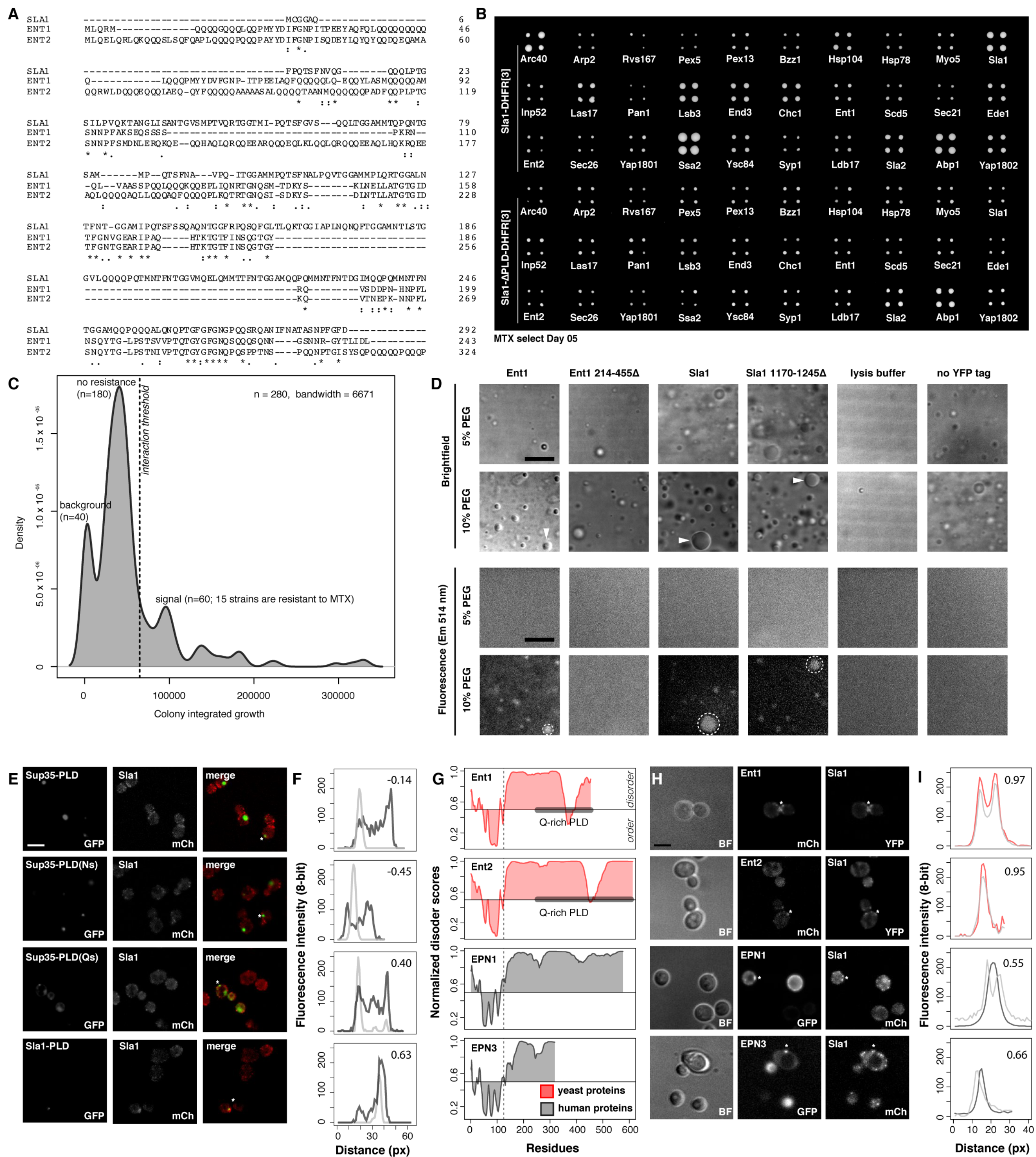

Supplementary Figure 3 | Colocalization of Sup35 NM sequence variants and human Epsin homologs expressed in yeast cells. Related to Figure 3. (A) Sequence alignment of Ent1, Ent2 and Sla1 PLDs with Clustal Omega. (B) DHFR-PCA and methotrexate (MTX) selection plate after 5 days of growth shows that the PLD deletion mutant of Sla1 loses most interactions of *wildtype* Sla1. (C) Density (number of colonies with given total pixel intensity) *versus* colony integrated

growth (total pixel intensity) after 5 days of MTX selection for DHFR reconstitution. Peaks are labeled with their corresponding measurements for plate background (n=40 empty spots), colonies with no resistance to MTX (n=180 colonies; 45 strains) and colonies that grow on MTX (n=60 colonies; 15 strains) above a selected integrated density threshold. We detected 13 interactions for full-length Sla1 protein and 2 interactions for the mutant Sla1 protein that do not contain the PLD. (D) *In vitro* droplet formation from cleared cell lysates that express Ent1-Venus YFP or Sla1-Venus YFP fluorescent full-length or PLD deletion mutants. Phase separation is assessed with addition of 5 or 10% PEG. Both brightfield and fluorescence images are shown. Arrows in brightfield images correspond to circled droplets in fluorescence channel. Scale bar 10 μM. (E) Expression of Sup35 NM sequence variants and Sla1 PLD with GFP fluorescent tag and assessment of their colocalization with Sla1 tagged with mCherry. Lines indicate spatial location for colocalization analysis of the respective signal (F) Line scans (performed as indicated with line in E) confirm, that neither Sup35 NM, Sup35 NM(N) with all Qs mutated to Ns nor Sup35 NM(Q) with all Ns mutated to Qs (black lines) colocalize with Sla1 foci (grey lines) in yeast cells, unlike Sla1 PLD (black) that colocalize with endogenous Sla1 proteins (grey). Pearson correlation values are given to confirm if the signals colocalize. Scale bar 5 μM. (G) PNDR-fit score (VLS2) for Ent1, Ent2, EPN1 and EPN3 proteins show conservation of the disorder along the sequence of these yeast (red) and human (grey) homologs. (H) Expression of each protein with indicated fluorescent tag and assessment of their colocalization with Sla1 tagged with a compatible fluorophore. Line indicates spatial location for colocalization analysis of the respective signal (I) Line scans (performed as indicated with lines in H) confirm that neither EPN1 nor EPN3 colocalize with Sla1 foci in yeast cells, unlike Ent1 and Ent2 that colocalize with Sla1. Pearson correlation values are given to confirm if the signals colocalize.

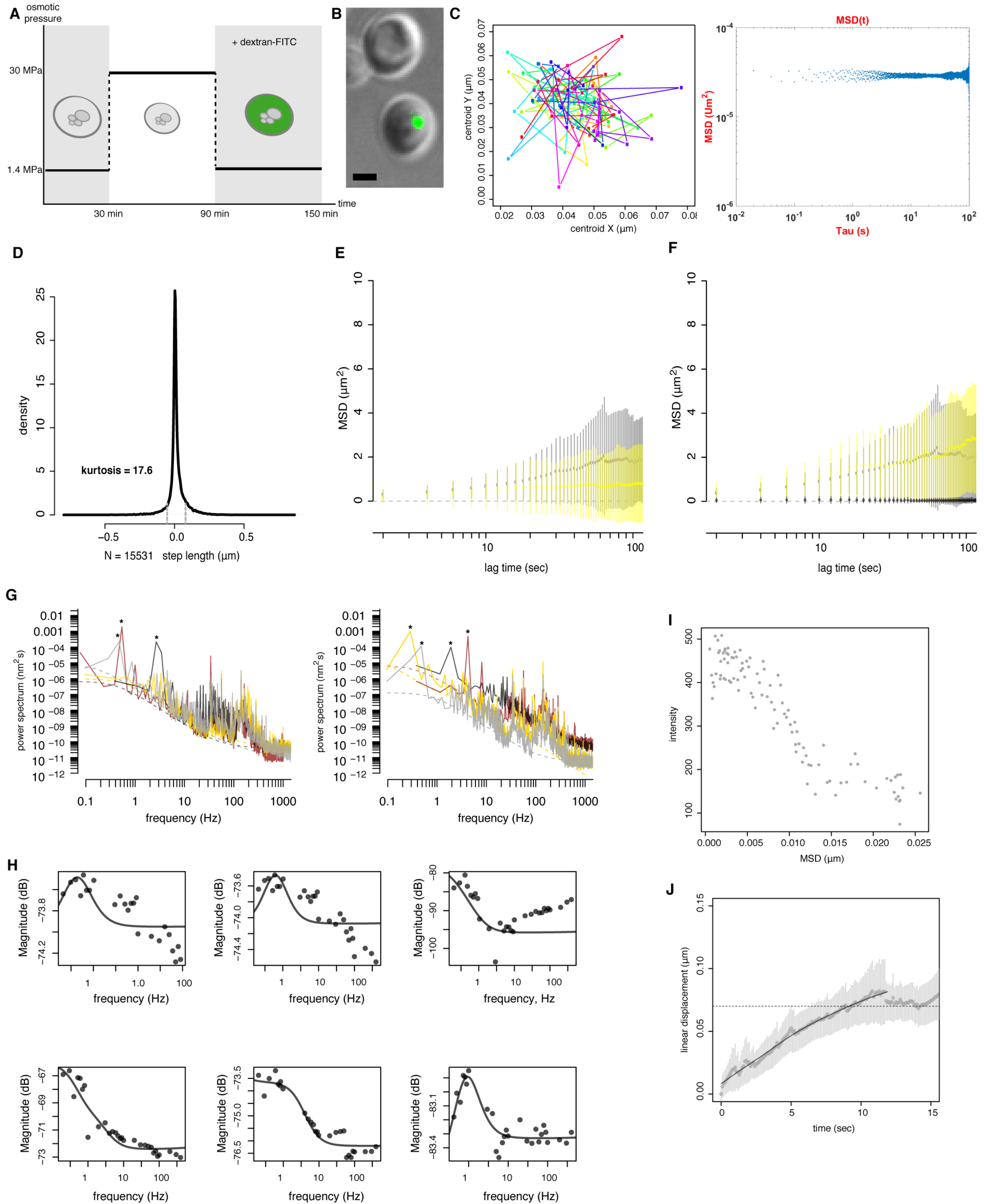

Supplementary Figure 4 | Osmoporation of polystyrene beads and dynamic mechanical analysis of cytosol with optical tweezers. Related to Figure 4. (A) Schematic representation of the two-

cycle osmotic shock used to osmoporate 200 nm polystyrene beads into haploid yeast *GPD1Δ* cells treated with Lat A. The osmoporation treatment induces a senescent-like state in most cells, but we could rescue a small fraction of cells that continue to divide in rich YPD medium. (B) Images of Sla2-Dronpa3 (green foci) cells with osmoporated beads (left panel). Scale bar is 2 µm. (C) Passive 2D displacement in x and y of 200 nm polystyrene beads measured based on centroid tracking. We observed the movement of beads by centroid tracking (middle panel) and also determined the mean square displacement (right panel). The polystyrene beads we incorporated into cells were confined within the cytosol with a MSD close to that of technical noise. (D) We measured displacement of expressed viral capsid microNS particles labeled with GFP in both untreated and osmoporated *GPD1Δ* cells. Distribution of step length of expressed microNS-GFP particles determined by centroid tracking in untreated cells. (E-F) MSD of microNS particles in untreated (grey) and osmoporated (yellow) cells as a function of lag time (seconds). Data points represent mean ± standard deviation of n = 300 traces in untreated *versus* osmoporated cells, panel b shows raw data and panel c shows data filtered for caged particles with MSD < 1 represented in black. (G) We measured the viscoelastic properties of the cytosol (of Lat A treated *GPD1Δ* cells) using the response of 200 nm polystyrene beads to sinusoidal oscillations of the tweezers and the high frequency domain of the power spectrum associated with thermal motions of the bead. Power spectra of samples are coded with distinct colors. Below frequencies of 500 Hz, the power spectra show fluctuations from tweezer oscillations (marked *), cellular processes and sample vibration. (H) Magnitude of the response (dB) of the bead displacement to sinusoidal oscillations of the optical trap position. Lines indicate global fits of the power spectra and response magnitudes to a model that describes the viscoelasticity of a crosslinked polymer network (Methods). (I) Centroid tracking within a confocal volume of Sla1-YFP foci in *GPD1Δ* mutant strains treated with Lat A. Single Sla1-YFP focus fluorescence intensity as a function of mean square displacement in a confocal volume as determine by spinning disk pinhole size. Images were acquired at 10 frames per second. Only foci with a decreasing fluorescence bleaching were selected to measure their displacement. (J) Linear displacement of Sla1 foci within a confocal volume as a function of time. Mean ± standard deviation of displacement is shown for n > 50 per time point. Total traces n = 275; note that traces do not have the same length. The average displacement is about 7.4 nm per second from polynomial fit (black curve). Horizontal dashed line indicates an invagination of 70 nm, minimal depth required for the constriction and scission steps.

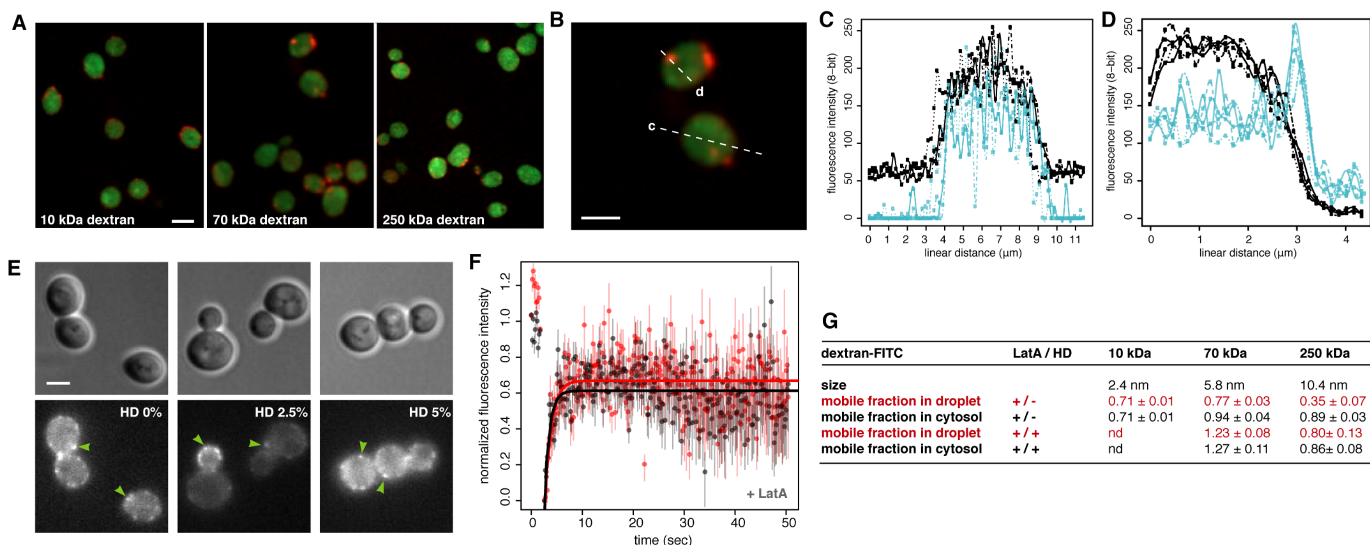

dextran-FITC	LatA / HD	10 kDa	70 kDa	250 kDa
size		2.4 nm	5.8 nm	10.4 nm
mobile fraction in droplet	+ / -	0.71 ± 0.01	0.77 ± 0.03	0.35 ± 0.07
mobile fraction in cytosol	+ / -	0.71 ± 0.01	0.94 ± 0.04	0.89 ± 0.03
mobile fraction in droplet	+ / +	nd	1.23 ± 0.08	0.80± 0.13
mobile fraction in cytosol	+ / +	nd	1.27 ± 0.11	0.86± 0.08

Supplementary Figure 5 | Colocalization of different sized dextran-FITC revealed that endocytic condensates exclude objects of diameters > 5.8 nm. Related to Figure 5. (A) 2-color fluorescent images of osmoporated dextran-FITC of different sizes in Sla1-mCherry treated with Lat A, Scale bar is 4 µm. (B) 2-color fluorescent images of dextran-FITC of 5.8 nm in size osmoporated into *GPD1Δ* Sla1-mCherry cells treated with Lat A, Scale bar is 4 µm. Examples of line scans (dashed) that were performed either outside (c) or across (d) Sla1-mCherry foci. (C) Multiple line scans of 5.8 nm dextran-FITC fluorescent signal (back) outside Sla1-mCherry cortical regions (blue). Fluorescence intensity patterns thus show the fluorescence of a line across the cytoplasm that doesn't include any concentrated foci of Sla1-mCherry. (D) Multiple line scans of 5.8 nm dextran-FITC fluorescent signal (back) within Sla1-mCherry cortical regions (blue) shows partial exclusion of these molecules. (E) Brigthfield and fluorescence images of *GPD1Δ* cells Syp1-mCherry cells treated with 05, 2.5 and 5% HD respectively, show that Syp1-mCherry foci are not dissolved by HD (arrows). (F) Fluorescence recovery after photobleaching (FRAP) of the bleached 2.4 nm dextran-FITC, respectively, within a Sla1-mCherry focus (red) and neighbouring cytosol regions (black) without Sla1 signal. *GPD1Δ* cells Sla1-mCherry were treated with 20 µM Lat A. Data points (mean ± SEM; n = 10 cells) were fitted to a single term recovery function (Methods). (G) Summary of mobile fractions determined for 2.4 nm, 5.8 nm and 10.4 nm dextran-FITC in either the endocytic condensate region or neighbour cytosol (mean ± se estimated from fits).

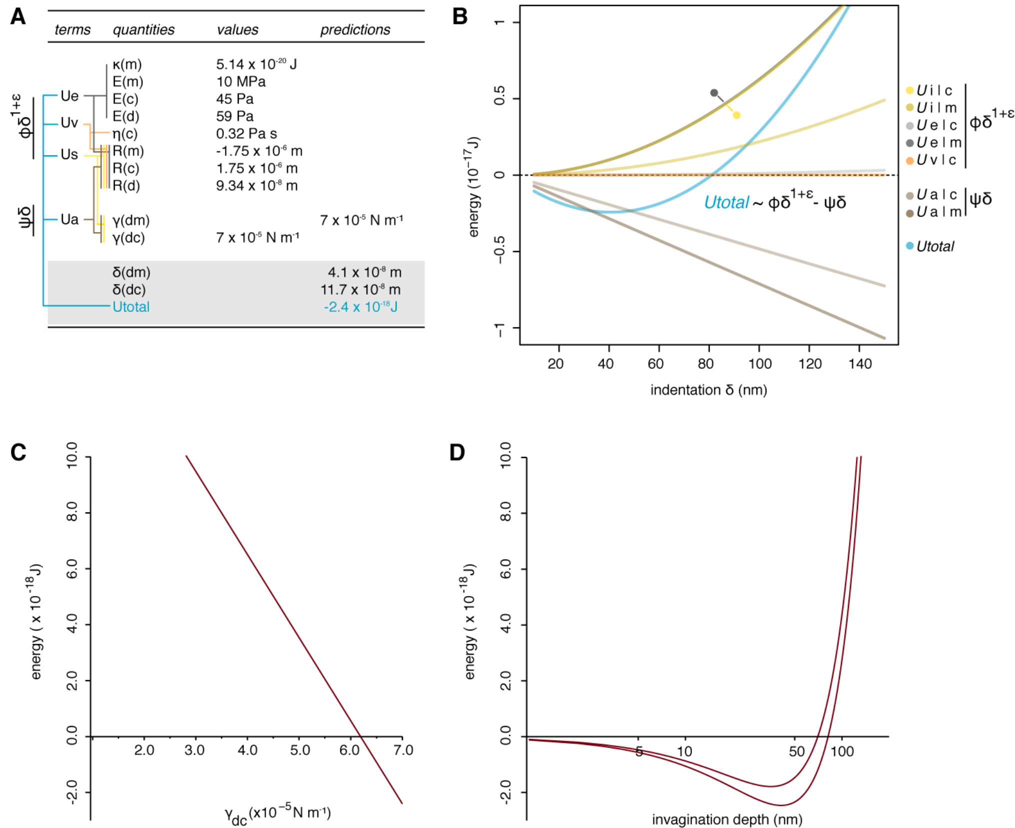

**Supplementary Figure 6 | ** Endocytic condensates apply mechanical stress that deform the membrane. Related to Figure 6 and Movie S2. (A) Values of bending, elastic, viscosity, surface tension and geometry quantities used in the calculation are recapitulated. Colour coded lines indicate which quantities were used to calculate the respective energies U_x, that in turn compose the ϕ and ψ terms of Equation 1. (B) Equation (1) (insert) was used to calculate the energy penalties and contributions at the cytosol and membrane interfaces with the endocytic condensate. Total energy of the system (blue), energy penalties (yellow, orange and grey) and energy contributions (brown) are presented as a function of membrane invagination (δ). Colour legend (right) specifies energy traces U_{xly}, where x= (E), elasticity or (v), viscosity of either the cytosol (c) or membrane (*m*) and (i) is interfacial tension and (a) is adhesion of cytosol or membrane with the endocytic condensate. Quantities used to calculate energies are detailed in Table S3 and S4. (C) Plot of total energy (y axis) as a function of condensate-cytosol surface tension (x axis) shows that the energy favorable values of γ_{dc} range between 6.2 x10^{-5} N•m^{-1} to 7 x10^{-5} N•m^{-1}. (D) 2D representation of the energy and depth accessible to a successful invagination. With the minimal (top curve) and maximal (lower curve) values of γ_{dm} our model predicts precise range of favorable δ (x axis) that minimizes total energy (y axis).

Supplementary Tables

Supplementary Table 1 | Strains used in this study

name	*genotype*	*source*
BY4741	MATa his3Δ1 leu2Δ0 met15Δ0 ura3Δ0	
GPD1Δ	BY4741 gpd1Δ::KanMX	YKO
Ent1-GFP	B4741 ent1-GFP::His3MX	GFP
Ent2-GFP	B4741 ent2-GFP::His3MX	GFP
Pan1-GFP	B4741 pan1-GFP::His3MX	GFP
Sla1-GFP	B4741 sla1-GFP::His3MX	GFP
Sla2-GFP	B4741 sla2-GFP::His3MX	GFP
Yap1801-GFP	B4741 yap1801-GFP::His3MX	GFP
Yap1802-GFP	B4741 yap1802-GFP::His3MX	GFP
Ent1-PLDΔ	BY4741 ent1-PLDΔ-Venus::HygMX	this study
Ent1-venus	B4741 ent1-Venus::HygMX	this study
Ent2-PLDΔ	BY4741 ent2-PLDΔ-Venus::HygMX	this study
Ent2-venus	B4741 ent2-Venus::HygMX	this study
ENT2Δ	BY4741 ent2Δ::KanMX	YKO
GPD1Δ Sla1- mCherry	GPD1Δ sla1-mCherry::HygMX	this study
GPD1Δ Sla1-venus	GPD1Δ sla1-venus::HygMX	this study
SLA1Δ	BY4741 sla1Δ::KanMX	YKO
GPD1Δ Syp1- mCherry	GPD1Δ syp1-mCherry::HygMX	this study
Sla1-GFP Abp1- mCherry	BY4741 sla1-GFP::His3MX abp1-mCherry::HygMX	this study
Sla1-mCherry	BY4741 sla1-mCherry::HygMX	this study
Sla1-PLDΔ	BY4741 sla1-PLDΔ-Venus::HygMX	this study
Sla1-venus	B4741 sla1-Venus::HygMX	this study
Sla2-GFP Sla1-mCherry	B4741 sla2-GFP::His3MX sla1-mCherry::HygMX	this study
Sup35-mCherry	BY4741 sup35-mCherry::HygMX	this study
Yap1801-PLDΔ	BY4741 yap1801f-PLDΔ-Venus::HygMX	this study
Yap1801-venus	B4741 yap1801-Venus::HygMX	this study
Yap1802-PLDΔ	BY4741 yap1802-PLDΔ-Venus::HygMX	this study
Yap1802-venus	B4741 yap1802-Venus::HygMX	this study

Supplementary Table 2 | Parameters and variables used in our model were either measured in this study or obtained from the literature

parameters	***definition***	***value***	***note***	***source***
E_m	membrane elastic modulus	1 x10^7 Pa	*estimate*	Landau 1986
κ_m	membrane bending modulus	12.5•K_BT		Harmandaris 2006
v_m	membrane poisson's ratio	0.45	*from 0.1 to 0.5*	Zhang 2013
δ_m	membrane indentation	5 x10^{-8} m	from 2.5 x 10^{-8} to 5 x 10^{-8} m	EM
R_m	membrane radius	-1.75 x 10^{-6} m	*negative curvature*	*this study*
E_c	cytosol elastic modulus	45 Pa	at 1 Hz	*this study*
η	cytosol viscosity	0.35 Pa•s^{-1}	*at 0.5 Hz*	*this study*
v_c	cytoplasm poisson's ratio	0.45	*from 0.1 to 0.5*	Zhang 2013
δ_c	indentation cytosol	1.18 x 10^{-7} m	±6 x 10^{-9}m	*this study*
R_c	membrane radius	1.75 x 10^{-6} m		*this study*
E_{drop}	droplet elastic modulus	59 Pa		*this study*
$2a_{drop}$	droplet contact diameter	2.09 x 10^{-7} m	±1 x 10^{-8}m	*this study*
δ_{drop}	indentation droplet	1.18 x 10^{-7} m	±6 x 10^{-9}m	*this study*
R_{drop}	droplet radius	9.3 x 10^{-7} m	~a^2/R	*Hertz*
θ	droplet contact angle	96.7°	$\theta = 2 \arctan(\delta_{drop} / a_{drop})$	Young

* EM refers to electron microscopy data (Kukulski, Picco et al. 2016) and Hertz refers to Hertz contact theory (Hertz 1882). Landau 1986 refers to estimation of membrane elastic modulus from the bending modulus and Poisson's ratio (Landau, Lifshits et al. 1986), Harmandaris 2006 (Harmandaris and Deserno 2006) and Zhang 2013 (Zhang, Soman et al. 2013).

Supplementary Table 3 | Constants and equations used in the elasto-adhesion model for the deformation of the membrane by protein droplets on cortical sites

variables	*definition*	*value*	*note*	**source**
mechanical stress method				
ε	mechanical deformation	*nd*	δ_x/R	Hooke
$\dot{\varepsilon}$	cytosol deformation rate	$0.004\ s^{-1}$		*this study*
E_{cell}	cell apparent elastic modulus	1000 Pa		AFM
σ	mechanical stress	1181Pa	$\sigma = \varepsilon E + \dot{\varepsilon}\eta$	Kelvin-Voigt
ΔP	pressure difference	1181Pa	$\Delta P = \sigma$	Laplace
H	interface mean curvature	$8.5\ x10^{6}\ m^{-1}$	1/R	Laplace
γ_{dc}	droplet-cytoplasm surface tension	$7\ x10^{-5} N{\bullet}m^{-1}$	$\gamma = \Delta P /(2H)$	Young-Laplace
elasto-adhesive contact method				
c	constant	0.92	$8/(5\sqrt{3})$	JKR
E^{*}_{dc}	cyto. vinterface equivalent elastic modulus	32 Pa	$1/E^{*}_{c} = (1-v_c^2)/E_c + (1-v_m^2)/E_m$	Hertz
E^{*}_{dm}	membrane interface equivalent elastic modulus	75 Pa		Hertz
R_{dm}	equivalent radius	$1.27\ x10^{-7}\ m$	$1/R = 1/R_m + 1/R_d$	Hertz
R_{dc}	equivalent radius	$1.11\ x10^{-7}\ m$	$1/R = 1/R_c + 1/R_d$	Hertz
δ_c	cytoplasm indentation	*see table S3*	$f(\delta_m) = \mu + \omega\delta_m$	*this study*
μ	constant	1.65		*this study*
k	constant	0		*this study*
W_{dm}	droplet-membrane work of adhesion	$6.15\ x10^{-5}\ N{\bullet}m^{-1}$	$W_{dm} = \gamma_{dc}(1+\cos\theta)$	Young Dupré
W_{dc}	droplet-cytosol work of adhesion	$6.15\ x10^{-5}\ N{\bullet}m^{-1}$	$= \gamma_{cm} + \gamma_{dm} - \gamma_{dc}$ predicted from model *(1* x 10^{-5} *to 7* x$10^{-5}N{\bullet}m^{-1}$*)*	*this study*
γ_{dm}	droplet-membrane surface tension	$6.15\ x10^{-5}\ N{\bullet}m^{-1}$	$\gamma_{dm} < \gamma_{dc}$ *(hydrophobic)* $\gamma_{dm} \sim (W_{dc} + \gamma_{dc})/2$	Young-Dupré
γ_{cm}	cytosol-membrane surface tension	$5.75\ x10^{-5}\ N{\bullet}m^{-1}$	$\gamma_{cm} = \gamma_{dm} + (\gamma_{dc}\cos\theta)$	Young

* not determined (nd). AFM refers to atomic force microscopy data from(Munder, Midtvedt et al. 2016).

Supplementary Table 4 | Summary of the indentations and energies predicted with our elasto-adhesive contact model

variable	*definition*	*value*	*in kT*	*source*
δ_m	membrane invagination	$4.06\ x10^{-8}$ m	*nd*	*this study*
δ_c	cytoplasm deformation	$1.17\ x10^{-7}$ m	*nd*	*this study*
U_{total}	total energy	$-2.4\ x10^{-18}$ J	*-590•kT*	*this study*
U_{penal}	total energy penalties	$2.4\ x10^{-18}$ J	*590•kT*	*this study*
U_{em}	corrected elastic energy at droplet-membrane interface	$1\ x10^{-18}$ J	250•*kT*	*this study*
U_{ec}	elastic energy at droplet-cytoplasm interface	$1.2\ x10^{-20}$ J	*3•kT*	*this study*
$U_{\gamma m}$	surface energy at droplet-membrane interface	$3.6\ x10^{-19}$ J	88•*kT*	*this study*
$U_{\gamma c}$	surface energy at droplet-cytoplasm interface	$1\ x10^{-18}$ J	*249•kT*	*this study*
U_{vc}	viscous friction energy	$2.5\ x10^{-21}$ J	1•kT	*this study*
U_{adh}	total adhesion energy	$4.9\ x10^{-18}$ J	1180•*kT*	*this study*
U_{am}	adhesion energy at droplet-membrane interface	$2\ x10^{-18}$ J	477•*kT*	*this study*
U_{ac}	adhesion energy at droplet-cytoplasm interface	$2.9\ x10^{18}$ J	703•*kT*	*this study*

Supplementary movies

Movie S1. Pulse-chase experiments with HD showed that HD-dependent dissolution of Sla1 puncta was reversible. 2-color time-lapse fluorescence images of Sla1-GFP Abp1-mCherry cells treated with HD-containing media at 10 min time point, and then with fresh media without HD at 15 min time point. Related to Figure 2.

Movie S2. Analogy of how endocytic condensates can generate a centered invagination of the membrane. Related to Figure 6.

Supplementary references

1. Alberti, S., R. Halfmann, O. King, A. Kapila and S. Lindquist (2009). "A systematic survey identifies prions and illuminates sequence features of prionogenic proteins." Cell **137**(1): 146-158.

2. Brangwynne, C. P., T. J. Mitchison and A. A. Hyman (2011). "Active liquid-like behavior of nucleoli determines their size and shape in Xenopus laevis oocytes." Proc Natl Acad Sci U S A **108**(11): 4334-4339.

3. Carlsson, A. E. and P. V. Bayly (2014). "Force generation by endocytic actin patches in budding yeast." Biophys J **106**(8): 1596-1606.

4. da Silva Pedrini, M. R., S. Dupont, A. de Anchieta Camara, Jr., L. Beney and P. Gervais (2014). "Osmoporation: a simple way to internalize hydrophilic molecules into yeast." Appl Microbiol Biotechnol **98**(3): 1271-1280.

5. Dill, K. A. and S. Bromberg (2011). Molecular driving forces : statistical thermodynamics in biology, chemistry, physics, and nanoscience. London ; New York, Garland Science.

6. Fischer, M., A. C. Richardson, S. N. Reihani, L. B. Oddershede and K. Berg-Sorensen (2010). "Active-passive calibration of optical tweezers in viscoelastic media." Rev Sci Instrum **81**(1): 015103.

7. Harmandaris, V. A. and M. Deserno (2006). "A novel method for measuring the bending rigidity of model lipid membranes by simulating tethers." J Chem Phys **125**(20): 204905.

8. Helfrich, W. (1973). "Elastic properties of lipid bilayers: theory and possible experiments." Z Naturforsch C **28**(11): 693-703.

9. Hendricks, A. G., E. L. Holzbaur and Y. E. Goldman (2012). "Force measurements on cargoes in living cells reveal collective dynamics of microtubule motors." Proc Natl Acad Sci U S A **109**(45): 18447-18452.

10. Hertz, H. R. (1882). Ueber die Beruehrung elastischer Koerper (On Contact Between Elastic Bodies). Leipzig, Germany, 1895.

11. Ho, C. H., L. Magtanong, S. L. Barker, D. Gresham, S. Nishimura, P. Natarajan, J. L. Koh, J. Porter,

C. A. Gray, R. J. Andersen, G. Giaever, C. Nislow, B. Andrews, D. Botstein, T. R. Graham, M. Yoshida and C. Boone (2009). "A molecular barcoded yeast ORF library enables mode-of-action analysis of bioactive compounds." Nat Biotechnol **27**(4): 369-377.

12. Huh, W. K., J. V. Falvo, L. C. Gerke, A. S. Carroll, R. W. Howson, J. S. Weissman and E. K. O'Shea (2003). "Global analysis of protein localization in budding yeast." Nature **425**(6959): 686-691.

13. Idrissi, F. Z., A. Blasco, A. Espinal and M. I. Geli (2012). "Ultrastructural dynamics of proteins involved in endocytic budding." Proc Natl Acad Sci U S A **109**(39): E2587-2594.

14. Idrissi, F. Z., H. Grotsch, I. M. Fernandez-Golbano, C. Presciatto-Baschong, H. Riezman and M. I. Geli (2008). "Distinct acto/myosin-I structures associate with endocytic profiles at the plasma membrane." J Cell Biol **180**(6): 1219-1232.

15. Johnson, K. L. K., K.;Roberts, A. D. (1971). "Surface energy and the contact of elastic solid." Proc. R. Soc. Lond. A. **324**: 301-313.

16. Koenderink, G. H., M. Atakhorrami, F. C. MacKintosh and C. F. Schmidt (2006). "High-frequency stress relaxation in semiflexible polymer solutions and networks." Phys Rev Lett **96**(13): 138307.

17. Kroschwald, S., S. Maharana, D. Mateju, L. Malinovska, E. Nuske, I. Poser, D. Richter and S. Alberti (2015). "Promiscuous interactions and protein disaggregases determine the material state of stress-inducible RNP granules." Elife **4**: e06807.

18. Kukulski, W., A. Picco, T. Specht, J. A. Briggs and M. Kaksonen (2016). "Clathrin modulates vesicle scission, but not invagination shape, in yeast endocytosis." Elife **5**.

19. Kukulski, W., M. Schorb, M. Kaksonen and J. A. Briggs (2012). "Plasma membrane reshaping during endocytosis is revealed by time-resolved electron tomography." Cell **150**(3): 508-520.

20. Landau, L. D., E. M. Lifshits, A. d. M. Kosevich and L. P. Pitaevskiæi (1986). Theory of elasticity. Oxford ; New York, Pergamon Press.

21. Lieleg, O., K. M. Schmoller, M. M. Claessens and A. R. Bausch (2009). "Cytoskeletal polymer networks: viscoelastic properties are determined by the microscopic interaction potential of cross-links." Biophys J **96**(11): 4725-4732.

22. Munder, M. C., D. Midtvedt, T. Franzmann, E. Nuske, O. Otto, M. Herbig, E. Ulbricht, P. Muller, A. Taubenberger, S. Maharana, L. Malinovska, D. Richter, J. Guck, V. Zaburdaev and S. Alberti (2016). "A pH-driven transition of the cytoplasm from a fluid- to a solid-like state promotes entry into dormancy." Elife **5**.

23. Ries, J., C. Kaplan, E. Platonova, H. Eghlidi and H. Ewers (2012). "A simple, versatile method for GFP-based super-resolution microscopy via nanobodies." Nat Methods **9**(6): 582-584.

24. Roman, B. and J. Bico (2010). "Elasto-capillarity: deforming an elastic structure with a liquid droplet." J Phys Condens Matter **22**(49): 493101.

25. Sheff, M. A. and K. S. Thorn (2004). "Optimized cassettes for fluorescent protein tagging in Saccharomyces cerevisiae." Yeast **21**(8): 661-670.

26. Style, R. W., C. Hyland, R. Boltyanskiy, J. S. Wettlaufer and E. R. Dufresne (2013). "Surface tension and contact with soft elastic solids." Nat Commun **4**: 2728.

27. Tarassov, K., V. Messier, C. R. Landry, S. Radinovic, M. M. Serna Molina, I. Shames, Y. Malitskaya, J. Vogel, H. Bussey and S. W. Michnick (2008). "An in vivo map of the yeast protein interactome." Science **320**(5882): 1465-1470.

28. Xue, B., R. L. Dunbrack, R. W. Williams, A. K. Dunker and V. N. Uversky (2010). "PONDR-FIT: a meta-predictor of intrinsically disordered amino acids." Biochim Biophys Acta **1804**(4): 996-1010.

29. Zhang, W., P. Soman, K. Meggs, X. Qu and S. Chen (2013). "Tuning the Poisson's Ratio of Biomaterials for Investigating Cellular Response." Adv Funct Mater **23**(25): 3226-3232.